Nuclear Science and Engineering

ISSN: (Print) (Online) Journal homepage: www.tandfonline.com/journals/unse20

Verification of Griffin-Pronghorn-Coupled Multiphysics Code System Against CNRS Molten Salt Reactor Benchmark

Mustafa K. Jaradat, Namjae Choi & Abdalla Abou-Jaoude

To cite this article: Mustafa K. Jaradat, Namjae Choi & Abdalla Abou-Jaoude (23 Feb 2024): Verification of Griffin-Pronghorn-Coupled Multiphysics Code System Against CNRS Molten Salt Reactor Benchmark, Nuclear Science and Engineering, DOI: 10.1080/00295639.2024.2306702

To link to this article: https://doi.org/10.1080/00295639.2024.2306702

Published online: 23 Feb 2024.

NUCLEAR SCIENCE AND ENGINEERING
DOI: https://doi.org/10.1080/00295639.2024.2306702

Verification of Griffin-Pronghorn-Coupled Multiphysics Code System Against CNRS Molten Salt Reactor Benchmark

Mustafa K. Jaradat, Namjae Choi,* and Abdalla Abou-Jaoude

Idaho National Laboratory, Department of Reactor Physics Methods and Analysis, 1955 Fremont Avenue, Idaho Falls, Idaho 83415

Received August 23, 2023
Accepted for Publication January 12, 2024

Abstract — *The molten salt reactor (MSR) flowing-fuel simulation capability of the Griffin-Pronghorn-coupled multiphysics code system developed by Idaho National Laboratory (INL) was verified against the Center National de la Recherche Scientifique (CNRS) MSR benchmark problem. Griffin and Pronghorn, which are INL's neutronics and thermal-hydraulics codes built upon the Multiphysics Object-Oriented Simulation Environment (MOOSE) framework, have been recently extended to handle the flowing fuel of MSRs causing the drift of delayed neutron precursors (DNP). In the Griffin-Pronghorn code system, Griffin provides the fission rate density to Pronghorn, which simulates the generation, decay, and transport of DNPs along with the fluid, and the redistributed DNP densities are fed back to Griffin. The coupling and transfers are largely automatically managed at the framework level by the powerful MultiApp system of MOOSE. The verification results against the CNRS benchmark problem demonstrate that the Griffin-Pronghorn code system can accurately simulate the unique physics phenomena of MSRs in both steady-state and transient conditions.*

Keywords — *Molten salt reactor, flowing fuel, delayed neutron precursors, Griffin, Pronghorn.*

Note — *Some figures may be in color only in the electronic version.*

I. INTRODUCTION

Molten salt reactors (MSRs), one of the Generation IV reactor concepts, offer a variety of compelling advantages over traditional light water reactors, such as compactness, higher operating temperature, fission product capture, and enhanced safety features, including low operating pressure, elimination of hydrogen evolution, and passive decay heat removal.[1] The history of MSRs dates back to the mid-twentieth century when the United States operated two research MSRs at Oak Ridge National Laboratory (ORNL): the Aircraft Reactor Experiment[2] and the Molten Salt Reactor Experiment (MSRE),[3] but their exploration did not lead to the commercialization of MSRs. However, the interest in these reactors has been rekindled in the past few years amid the growing worldwide interest in small modular reactors. New MSR designs and deployment plans are springing up around the world. Consequently, the necessity and demand for modeling and simulation tools for MSRs to support the design and regulatory processes are higher than ever.

Molten salt reactors with flowing fuel are unique in the sense that they utilize the fuel salt for both heat generation and extraction. This movement of fuel salt within the primary loop results in a partial decay of

*E-mail: Namjae.Choi@inl.gov

delayed neutron precursors (DNPs) outside the core region. This results in a strong coupling between neutronics and thermal hydraulics, which requires coupled multiphysics modeling and simulation to capture these effects. Thus, neutronics and thermal-hydraulic codes need to be extended to handle the strongly coupled physics and the accompanied DNPs transport.

Several efforts have been devoted to developing multiphysics tools for MSR modeling and simulation. In the 1960s, ORNL developed a modified point kinetics model for circulating fuel with a heat transfer model using a multinode approach and performed dynamic analysis of the MSRE.[4] In the early 2000s, there were several activities for MSR modeling in Europe, where a thermal spectrum MSR benchmark was developed based on some of the MSRE experiment results under the Molten Salt reactor Technology, or MOST, project,[5] with several simplifications. Also, a preconceptual design and steady-state analysis of a fast spectrum MSR benchmark with fluoride-based salt were made under the Evaluation and Viability of Liquid fuel fast reactor system, or EVOL, project,[6] which attracted large attention for breeding and actinides burning feasibility.[7] TerraPower proposed the Molten Chloride Faster Reactor (MCFR)[8] with a similar concept to the European Molten Salt Fast Reactor (MSFR).

Several tools have been developed to pursue the modeling and safety analysis of MSRs with both thermal and fast spectrums, such as SIMMER-III,[9] Cinsf1D,[10] DYN3D-MSR,[11] MOREL,[12] COMSOL,[13] DALTON-HEAT,[14,15] PARCS-TRACE,[16] OpenFOAM,[17,18] and ARC.[19] In the United States, several code systems have been developed recently for MSR analysis ranging from simple point kinetics models to multiphysics-coupled models, such as SAM,[20] Moltres,[21] PROTEUS-NODAL,[22–24] and PROTEUS-NODAL-SAM.[25,26]

Idaho National Laboratory (INL) has made numerous efforts to develop modeling and simulation tools for advanced reactors to serve its mission of supporting the deployment of advanced reactors, including MSRs. As one of the efforts, INL's neutronics code Griffin[27] and thermal-hydraulic code Pronghorn[28] were built upon the Multiphysics Object-Oriented Simulation Environment (MOOSE) framework.[29] These codes have been recently extended to handle the flowing-fuel of MSRs, which involves the drift of DNPs, and this capability is being actively verified against benchmark problems,[30–32] including the MSR benchmark problem proposed by the Center National de la Recherche Scientifique (CNRS).[33] Validation efforts against an actual experiment are also ongoing based on the available experimental data from the MSRE.[34]

This work presents the complete analysis of the CNRS benchmark problem with the Griffin-Pronghorn code system of INL. While some of the previous work tackled only initial parts of the problem using older capabilities in Griffin-Pronghorn.[32] This paper provides detailed and comprehensive results of the tools for this verification problem. The following section starts by providing a description of the Griffin-Pronghorn code system and the CNRS benchmark. Then the benchmark analysis results using the Griffin-Pronghorn code system encompassing single and multiphysics steady-state, and transient problems is demonstrated in comparison with other benchmark participants' results, followed by a conclusion and summary.

II. CODE AND BENCHMARK DESCRIPTION

This section introduces the methodologies of the Griffin-Pronghorn-coupled code system built on the MOOSE[29] framework focusing on the MSR application. Also, a brief description of the CNRS benchmark specifications and geometry, as well as the inputs and observables of each benchmark step are provided.

The tools showcased here are all part of the MOOSE ecosystem. MOOSE provides simple, adaptive, and flexible interfaces for the specification of partial differential equations (PDEs), boundary conditions, and material properties. The framework internally handles all the parallelization and discretization for finite element methods (FEMs) and finite volume methods (FVMs).

The tools are developed under a rigorous software quality assurance (SQA) program that is compliant with the Nuclear Quality Assurance 1 (NQA-1) standards. This is expected to be invaluable to U.S.-based efforts to model MSRs. All MOOSE-based applications adopt a seamless and continuous development approach. The MOOSE framework also provides in-code documentation, ensuring the codes stay up to date. The framework automates the NQA-1 testing process, reducing the overhead of becoming and remaining NQA-1 compliant. Griffin and Pronghorn are both built on top of the MOOSE framework, and therefore inherit the entire SQA process.

The main driver for using the MOOSE framework, however, is its ability to effectively couple various physical phenomena under a single computational run. MOOSE allows for simultaneous execution of multiple MOOSE-based applications with data transfers through the MultiApp capability and also provides numerical algorithms to couple the subapplications. MOOSE supports two iterative, nonlinear coupling schemes to solve

coupled PDEs: operator-splitting scheme via Picard iteration and full coupling scheme via the Jacobian-Free Newton-Krylov (JFNK) method.[35] In this work, the Picard iteration scheme is employed to converge the nonlinearities in the Griffin-Pronghorn code system. In theory, the JFNK method can converge a nonlinear problem in fewer iterations and can be more robust than the Picard iteration scheme, but it has practical issues in the actual application in that it requires building a single system evaluating every physics simultaneously. Building a fully consistent single system for multiple physics is often very difficult, if not impossible, especially when each physics code has been independently developed and uses different schemes. As such, the Picard iteration scheme is adopted owing to its simplicity and flexibility.

II.A. Griffin-Pronghorn Code System

Griffin is a MOOSE-based deterministic radiation transport and reactor multiphysics application that integrates the technologies developed in Rattlesnake,[36] Mammoth,[37] PROTEUS,[38] and MC^2-3[39] for non-light-water advanced reactor technologies. Griffin solves various forms of the linear Boltzmann transport equation for the radiation flux distribution defined in time, space, direction, and energy. Griffin utilizes finite element unstructured mesh with the multigroup approximation and can choose among different angular discretization schemes [discrete ordinates (SN), spherical harmonics expansion, and diffusion approximations] to solve fixed-source, eigenvalue, and transient problems.

In this work, Griffin's diffusion solver is utilized, which is sufficient, as the benchmark deals with a homogeneous geometry. The multigroup neutron diffusion equation is given as

$$\begin{aligned}\frac{1}{v_g}\frac{\partial \phi_g}{\partial t} - \nabla \cdot D_g \nabla \phi_g + \Sigma_{t,g}\phi_g \\ = \sum_{g'=1}^{G} \Sigma_{s,g'\to g}\phi_{g'} + \frac{(1-\beta)\chi_{p,g}}{k_{eff}} \sum_{g'=1}^{G} \overline{\nu}\Sigma_{f,g'}\phi_{g'} \\ + \sum_{k=1}^{K} \chi^k_{d,g}\lambda_k C_k, \quad g = 1,\ 2,\ \cdots,\ G \quad ,\end{aligned} \tag{1}$$

where the term $\sum_{k=1}^{K} \chi^k_{d,g}\lambda_k C_k$ represents the delayed neutron source, which can be determined by solving the DNP concentration equations. MSRs with flowing fuel introduce an extra term to the DNP equations to account for the drift of DNPs in the core, and their decay outside the core as given in Eq. (2),

$$\begin{aligned}\frac{\partial C_k}{\partial t} + \nabla \cdot (\vec{u} C_k) + \lambda_k C_k \\ = \frac{\beta_k}{k_{eff}} \sum_{g'=1}^{G} \overline{\nu}|\Sigma_{f,g'}\phi_{g'}, \quad k = 1,\ 2,\ \cdots,\ K \quad ,\end{aligned} \tag{2}$$

where the term $\nabla \cdot (\vec{u} C_k)$ accounts for the drift of the DNPs within the core region.

Equation (2) is solved along with the homogenous boundary condition to determine the concentrations of the DNPs at the core inlet, taking into account their decay while residing in the outer loop. Equation (2) is strongly coupled to Eq. (1) given the velocity field and ex-core residence time, or tightly coupled by providing the DNP distributions as an external source, which requires multiphysics coupling to a thermal-fluids code. In the current work, the distribution of DNPs is obtained from Pronghorn with passive scalar solution capability.

Pronghorn is another MOOSE-based application for coarse-mesh thermal-hydraulic calculations. Pronghorn solves multidimensional compressible/incompressible Euler equations (leveraging the MOOSE Navier-Stokes module[40]) for porous and nonporous flow configurations. Pronghorn also has an additional capability to model the transport of DNPs with advection through the system, which is required for flowing-fuel MSRs to obtain the delayed neutron source distribution. The incompressible Navier-Stokes fluid flow base equations for MSRs are given by

$$\nabla \cdot \vec{u} = 0 \quad , \tag{3}$$

$$\begin{aligned}\frac{\partial \vec{u}}{\partial t} + \vec{u} \cdot \nabla \vec{u} = -\frac{1}{\rho_0}\nabla p + \nu \nabla^2 \vec{u} \\ + \vec{g}(1 - \alpha(T - T_0)) \quad ,\end{aligned} \tag{4}$$

$$\rho_0 c_p \frac{\partial T}{\partial t} + \rho_0 c_p \vec{u} \cdot \nabla T = \kappa_f \nabla^2 T + q''' \quad . \tag{5}$$

The thermal fluid equations, Eqs. (3), (4), and (5), are discretized using FVM, where the finite volume variables are constant monomials at the center of each element, and the face values are calculated using the first-order upwind

interpolation scheme for advected quantities, along with Rhie-Chow interpolation for velocities.[41]

Also, Pronghorn solves the passive scalar equation for DNP transport given the neutron fission source and decay constant of each delayed neutron family or group at the center of each element with an additional term to account for turbulence mixing as described in Eq. (6),

$$\frac{\partial \overline{C}_k}{\partial t} + \overline{\vec{u}} \cdot \nabla \overline{C}_k + \lambda_k \overline{C}_k - D\nabla^2 \overline{C}_k = \overline{S}_k, \quad k = 1, 2, \cdots, K \quad , \tag{6}$$

where the salt diffusion coefficient is related to the Schmidt number, which accounts for the turbulent diffusivity of the salt.

The coupling scheme of Griffin-Pronghorn under the MOOSE framework used in this work for MSR analysis is shown in Fig. 1. Griffin is the main application, and it provides the power density and fission source to Pronghorn (the subapplication) to obtain the temperature, density, velocity, and pressure fields, as well as the DNP distribution. The temperature field is transferred to Griffin to update the multigroup cross sections for incorporating thermal feedback. The DNP distribution is used to construct the total fission source to obtain the neutron flux solution and corresponding power density, which is fed back again to the Pronghorn calculations.

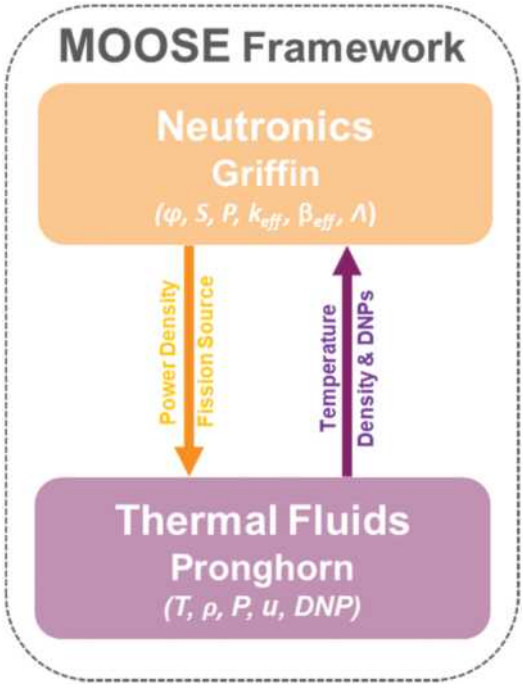

Fig. 1. Griffin-Pronghorn multiphysics coupling scheme for MSR analysis.

Since Pronghorn employs the FVM, all the transferred quantities between Griffin and Pronghorn should be cell averaged. Therefore, the DNP distribution and temperature that are transferred from Pronghorn are simply treated as constant monomial variables in Griffin. On the other hand, when transferring the power density and fission source to Pronghorn, which are linear variables, they are projected to constant monomial variables by taking the average. This process is handled by the MOOSE projection transfer system.

The parameters are exchanged between the two codes at each iteration to obtain a fully converged solution, and the convergence of the global Picard iteration is checked based on the relative reduction of the flux residual of Griffin. The feedback mechanisms captured by this multiphysics coupling of Griffin-Pronghorn are related to the cross-section changes by temperature and density and the DNP distribution changes by velocity.

II.B. Benchmark Description

The benchmark problem was originally developed for the numerical verification of thermal-hydraulic codes for incompressible flow in a lid-driven cavity.[42] It was recently extended for application to the fast spectrum MSR benchmark developed by LPSC/CNRS-Grenoble,[42,43] known as the CNRS benchmark,[33] considering multiphysics coupling of neutronics and thermal-hydraulic codes. The benchmark is used to verify modeling approaches of coupled multiphysics codes for MSR steady-state and transient analyses. The original benchmark participants were the Paul Scherrer Institute (PSI), Delft University of Technology (TUD), Politecnico di Milano (PoliMi), and CNRS. All the benchmark participants are listed in Table I along with the solution methods and codes used.

The geometry of the CNRS benchmark represents a simple two-dimensional, lid-driven cavity of a 2 × 2-m domain bare reactor with a homogenous fuel composition. The outer loop is not included in this benchmark; namely, the benchmark does not test the transition from the core to the ex-core regions. For a pointwise comparison of the observables, two centerlines were identified along radial (AA′) and axial (BB′) directions, as shown in Fig. 2. The cavity is filled with fluoride salt composed of ^{6}Li, ^{7}Li, ^{9}Be, ^{19}F, and ^{235}U as the fissile isotope with atomic fractions of 2.11%, 26.08%, 14.10%, 56.40%, and 1.31%, respectively.

The multigroup cross-section data and delayed neutron data of the fuel salt are provided by the benchmark in six energy groups and eight DNP groups, respectively,

TABLE I

Summary of the Benchmark Participants' Code Packages and Solution Methods

Participant	Neutronics Code/ Method	Thermal-Hydraulic Code	Numerical Method	Mesh
CNRS[44]	OpenFOAM/SP1 and SP3	OpenFOAM	Finite volume	Nonuniform 200 × 200
PoliMi[45]	OpenFOAM/Diffusion	OpenFOAM	Finite volume	Uniform 400 × 400
PSI[46]	GeN-FOAM/Diffusion	GeN-FOAM	Finite volume	Nonuniform 200 × 200
TUD[47]	PHANTOM/SN	DGFlows	Discontinuous finite element	Uniform 50 × 50
INL[a]	Griffin/Diffusion	Pronghorn	Continuous finite element (Griffin) finite volume (Pronghorn)	Uniform 200 × 200

[a]Current work institution: INL.

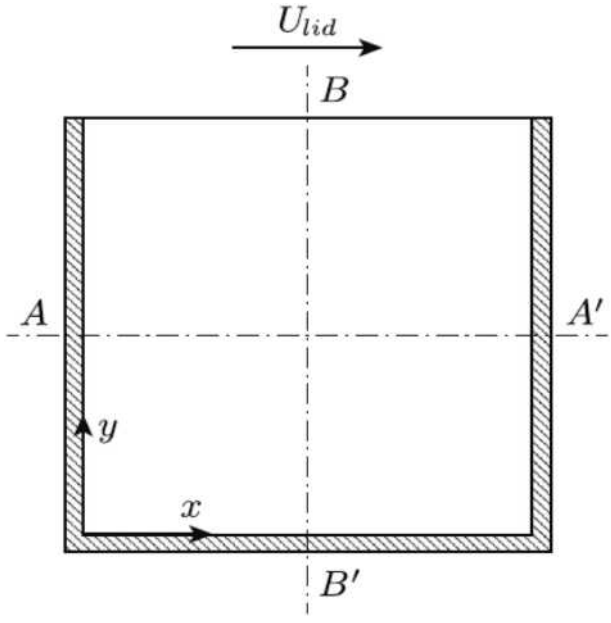

Fig. 2. CNRS benchmark problem geometry.[33]

which were generated at a single temperature of T_0 = 900 K. The delayed neutron fractions and decay constants of each precursor group are provided in Table II.

As the cross sections were generated only at a single temperature, the Doppler effect on the cross sections is neglected, and the thermal feedback only occurs by the fuel salt density changes as follows:

$$\Sigma_x(T) = \Sigma_x(T_0)\frac{\rho(T)}{\rho(T_0)} \quad , \tag{7}$$

where the fuel salt density changes linearly with respect to the temperature as

TABLE II

Delayed Neutron Data of the Fuel Salt[33]

Group	λ_k (s^{-1})	β_k (pcm)
1	0.0124667	24.2173
2	0.0282917	120.029
3	0.0425244	49.7887
4	0.133042	136.834
5	0.292467	185.916
6	0.666488	61.9812
7	1.634780	57.9049
8	3.554600	17.1090

$$\rho(T) = \rho(T_0)(1 - \alpha(T - T_0)) \quad , \tag{8}$$

with α being the thermal expansion coefficient.

The following boundary conditions were used to perform the neutronics and thermal-hydraulic calculations: (1) vacuum boundary conditions for neutron flux calculations at all boundaries, (2) a homogeneous Neumann boundary condition for the DNPs, (3) no-slip boundary conditions for velocity calculations at all boundaries except the top boundary (the lid), where forced flow was imposed in the form of lid-driven velocity, and (4) adiabatic boundary conditions for temperature calculations with volumetric heat sink for salt cooling defined as

$$q''' = \gamma(T_0 - T) \tag{9}$$

where γ is the heat transfer coefficient.

The fuel is considered as an incompressible laminar flow in the problem domain with only density changes affecting the buoyancy term, as given by Eq. (8) (the Boussinesq approximation). The fuel salt thermophysical

TABLE III

Fuel Salt Thermophysical Properties[33]

Property	Value
Density (kg/m^3)	2.0×10^3
Kinematic viscosity (m^2/s)	2.5×10^{-2}
Volumetric heat capacity (J/m^3/K)	6.15×10^6
Thermal expansion coefficient (1/K)	2.0×10^{-4}
Prandtl number	3.075×10^5
Schmidt number	2.0×10^8

properties specified by the benchmark are summarized in Table III.

The benchmark analysis is performed in three phases with progressively increasing complexity. Each phase is composed of one or more steps: single physics (standalone neutronics or thermal hydraulics) steady-state analysis (phase 0), multiphysics-coupled steady-state analysis (phase 1), and multiphysics-coupled transient analysis (phase 2). The input parameters and observables of each benchmark step are summarized in Table IV.

II.B.1. Phase 0: Single Physics Steady State

This phase verifies single physics steady-state calculations and is composed of three steps. Namely, this phase is intended to confirm the soundness of each code before performing coupled calculations. Step 0.1 compares the steady-state velocity field of the fuel salt for a given fixed lid velocity of 0.5 m/s. Step 0.2 compares the steady-state neutronics solutions. Step 0.3 compares the steady-state temperature profile with the velocity field of step 0.1 and the heat source of step 0.2 as inputs.

II.B.2. Phase 1: Steady-State Multiphysics Coupling

This phase focuses on verifying the multiphysics-coupled, steady-state calculations and comprises four steps. Step 1.1 assesses the impact of DNP drift on the reactivity and the delayed neutron source distribution with the fixed velocity field from step 0.1 and the constant temperature of 900 K. Step 1.2 adds in the temperature feedback to step 1.1 and assesses its impact on the reactivity and fission rate density distribution. Step 1.3 assesses the ability to perform a fully coupled simulation, including the velocity fields for a system without forced convection; namely, the lid velocity being zero, where the flow is only driven by the buoyancy effect caused by the temperature gradient. Finally, step 1.4 assesses fully coupled simulations for various combinations of reactor power and lid velocity, which is basically the generalization of step 1.3.

II.B.3. Phase 2: Time-Dependent Multiphysics Coupling

This phase is dedicated to verifying multiphysics-coupled transient calculations and is a single-step phase.

TABLE IV

Summary of Input Parameters and Observables of Each Benchmark Step

Step	Input Parameter	Observable
0.1	U_{lid} = 0.5 m/s	Velocity components along AA′ and BB′
0.2	T = 900 K, P = 1.0 GW	Fission rate density along AA′, reactivity
0.3	Fixed flow field from step 0.1, fixed heat source distribution from step 0.2, γ = 1.0 MW/m^3/K	Temperature along AA′ and BB′
1.1	Fixed flow field from step 0.1, T = 900 K, P = 1.0 GW	Delayed neutron source along AA′ and BB′, reactivity change from step 0.2, $\Delta\rho = \rho - \rho_{0.2}$
1.2	Fixed flow field from step 0.1, P = 1.0 GW, γ = 1.0 MW/m^3/K	Temperature distribution along AA′ and BB′, reactivity change from step 1.1, $\Delta\rho = \rho - \rho_{1.1}$, change of fission rate density along AA′ and BB′ with respect to the solution obtained at step 0.2
1.3	P = 1.0 GW, U_{lid} = 0.0 m/s, γ = 1.0 MW/m^3/K	Velocity components and temperature along AA′ and BB′, delayed neutron source along AA′ and BB′, reactivity change from step 0.2, $\Delta\rho = \rho - \rho_{0.2}$
1.4	γ = 1.0 MW/m^3/K, P variable in the range [0,1] GW, with a step of 0.2 GW, U_{lid} variable in the range [0, 0.5] m/s, with a step of 0.1 m/s	Reactivity change from step 0.2, $\Delta\rho = \rho - \rho_{0.2}$, as a function of P and U_{lid}
2.1	Steady-state solution from step 1.4 with U_{lid} = 0.5 m/s and P = 1.0 GW, γ = 1.0 MW/m^3/K	Power gain and phase shift as a function of the perturbation frequency

In this phase, the heat transfer coefficient is changed in time by a sinusoidal perturbation with an amplitude 10% of the original value and with varying frequencies f of 0.0125, 0.025, 0.05, 0.1, 0.2, 0.4, and 0.8 Hz as

$$\gamma = \gamma_0(1 + 0.1 \sin(2\pi f)) \tag{10}$$

where γ_0 is the reference volumetric heat transfer coefficient with value of 1×10^6 W/m^3/K. This leads to a sinusoidal behavior of the reactor power from which the power gain and the phase shift of power from the heat transfer coefficient can be computed. The power gain G is defined as

$$G(f) = \frac{P_{\max}(f)/P_{\text{avg}}(f) - 1}{\gamma_{\max}(f)/\gamma_{\text{avg}}(f) - 1} \quad . \tag{11}$$

III. RESULTS

In this section, the Griffin-Pronghorn solutions of each phase and step are presented in comparison to the results of other benchmark participants' codes. The simple average of the reference codes' results is taken as the reference solutions. The average discrepancy Δ_{avg} of a field quantity, which is a representative value for describing the overall discrepancy, is defined as[33]

$$\Delta_{\text{avg}} = \sqrt{\frac{\sum (Q - Q_{\text{avg}})^2}{\sum Q_{\text{avg}}^2}} \tag{12}$$

where Q and Q_{avg} are the solutions of each code and the average of reference codes, respectively, sampled in 0.01-m intervals along each centerline.

This results in mixing the diffusion and transport solutions. Nevertheless, it is considered reasonable as the problem is homogeneous, which makes fission source distributions largely unaffected by the angular discretization scheme. The average discrepancies of Griffin-Pronghorn are compared to the average discrepancies of the reference codes. The average discrepancy of each reference code is the discrepancy against other reference codes. Namely, when computing the average discrepancy of a reference code, the solutions of that code as well as the Griffin-Pronghorn solutions are not included in the average. If the average discrepancies of Griffin-Pronghorn are comparable with the range of the reference codes' average discrepancies, it can be concluded that the Griffin-Pronghorn solutions are consistent with the reference codes.

The benchmark also compares the pointwise solutions at a few equidistantly selected points with 0.25-m spacing along the centerlines, including boundaries. However, Pronghorn employs the FVM, which only provides the cell-averaged values at the boundary elements. Namely, the face values at the boundaries are not available. Also, there is no point in comparing the boundary values in the case of the velocity components, which should always have identical values with the boundary conditions. Therefore, the solutions at the points nearest to the boundaries are compared instead. The boundary values are also not included in computing the average discrepancies.

III.A. Phase 0: Single Physics Benchmark

III.A.1. Step 0.1: Velocity Field

The horizontal and vertical velocity components at the selected points along the centerlines are compared in Tables V and VI, respectively, and Figs. 3 and 4 show their full distributions along the centerlines. There is a significant difference in the vertical velocity component at the left boundary of BB′, but this is simply due to the very small magnitude of the values and the negative value of TUD, which distorts the average. The average discrepancies of Pronghorn fall within the range of the reference codes' average discrepancies or are lower than those, as shown in Table VII.

The vertical velocity component along BB′ shows a relatively higher average discrepancy due to a noticeable discrepancy around the peak. In that region, Pronghorn agrees well with PSI, but deviates from the other three codes. This is incurred by a steep gradient of the vertical velocity component around the region, as illustrated in the left image in Fig. 5, which can be affected sensitively by the differences in discretization schemes. The right image in Fig. 5 shows that refining the mesh in Pronghorn has a nonnegligible effect locally to the solution around the peak and that refined meshes give closer results to the reference codes other than PSI. However, refining the mesh entails a significant run time increase.

The run time of the 200 × 200 mesh case is approximately 1 min with 48 CPU cores on the INL Sawtooth cluster (Intel Xeon Platinum 8268), but those of the 400 × 400 and 800 × 800 mesh cases increase to 6.3 min and 46.9 min, respectively. In the Griffin-Pronghorn-coupled calculations that will be presented in

TABLE V

Step 0.1—Horizontal Velocity Component at Selected Points Along AA′ and BB′*

Point (m)	0.01	0.25	0.5	0.75	1	1.25	1.5	1.75	1.99
Code	AA′								
CNRS	−4.577E-05	−1.924E-02	−5.372E-02	−8.369E-02	−1.025E-01	−1.043E-01	−7.972E-02	−3.080E-02	−7.046E-05
PoliMi	−4.173E-05	−1.922E-02	−5.365E-02	−8.357E-02	−1.023E-01	−1.041E-01	−7.947E-02	−3.066E-02	−6.391E-05
PSI	−4.623E-05	−1.929E-02	−5.366E-02	−8.332E-02	−1.018E-01	−1.034E-01	−7.912E-02	−3.072E-02	−7.088E-05
TUD	−4.361E-05	−1.922E-02	−5.372E-02	−8.371E-02	−1.025E-01	−1.044E-01	−7.977E-02	−3.081E-02	−6.877E-05
Average	−4.434E-05	−1.924E-02	−5.369E-02	−8.357E-02	−1.023E-01	−1.040E-01	−7.952E-02	−3.075E-02	−6.850E-05
Pronghorn	−4.242E-05	−1.928E-02	−5.369E-02	−8.343E-02	−1.019E-01	−1.036E-01	−7.925E-02	−3.075E-02	−6.488E-05
Difference (%)	−4.32	0.23	0.00	−0.18	−0.32	−0.42	−0.34	0.01	−5.29
Code	BB′								
CNRS	−1.753E-03	−3.518E-02	−6.242E-02	−8.720E-02	−1.025E-01	−8.766E-02	−1.147E-02	1.717E-01	4.851E-01
PoliMi	−1.707E-03	−3.423E-02	−6.107E-02	−8.613E-02	−1.023E-01	−8.861E-02	−1.299E-02	1.706E-01	4.851E-01
PSI	−1.753E-03	−3.511E-02	−6.217E-02	−8.667E-02	−1.018E-01	−8.731E-02	−1.191E-02	1.705E-01	4.850E-01
TUD	−1.751E-03	−3.519E-02	−6.244E-02	−8.724E-02	−1.025E-01	−8.770E-02	−1.146E-02	1.718E-01	4.851E-01
Average	−1.741E-03	−3.492E-02	−6.203E-02	−8.681E-02	−1.023E-01	−8.782E-02	−1.196E-02	1.711E-01	4.851E-01
Pronghorn	−1.756E-03	−3.518E-02	−6.229E-02	−8.684E-02	−1.019E-01	−8.731E-02	−1.166E-02	1.708E-01	4.850E-01
Difference (%)	0.84	0.73	0.43	0.04	−0.32	−0.59	−2.48	−0.22	−0.01

*Horizontal velocity component in m/s.

TABLE VI

Step 0.1—Vertical Velocity Component at Selected Points Along AA′ and BB′*

Point (m)	0.01	0.25	0.5	0.75	1	1.25	1.5	1.75	1.99
Code	AA′								
CNRS	4.235E-03	7.266E-02	8.575E-02	6.084E-02	1.251E-02	−4.789E-02	−9.606E-02	−8.722E-02	−4.497E-03
PoliMi	4.158E-03	7.139E-02	8.433E-02	6.007E-02	1.269E-02	−4.691E-02	−9.472E-02	−8.621E-02	−4.445E-03
PSI	4.240E-03	7.265E-02	8.534E-02	6.021E-02	1.230E-02	−4.734E-02	−9.536E-02	−8.720E-02	−4.513E-03
TUD	4.233E-03	7.269E-02	8.580E-02	6.089E-02	1.252E-02	−4.794E-02	−9.613E-02	−8.726E-02	−4.496E-03
Average	4.216E-03	7.235E-02	8.531E-02	6.050E-02	1.250E-02	−4.752E-02	−9.557E-02	−8.697E-02	−4.488E-03
Pronghorn	4.244E-03	7.272E-02	8.550E-02	6.042E-02	1.230E-02	−4.756E-02	−9.554E-02	−8.724E-02	−4.511E-03
Difference (%)	0.66	0.52	0.23	−0.14	−1.62	0.09	−0.03	0.31	0.53
Code	BB′								
CNRS	2.947E-07	5.641E-05	6.309E-04	3.862E-03	1.251E-02	2.524E-02	3.048E-02	1.500E-02	2.664E-05
PoliMi	3.272E-07	9.118E-05	7.484E-04	4.046E-03	1.269E-02	2.534E-02	3.050E-02	1.500E-02	2.437E-05
PSI	3.504E-07	7.727E-05	6.822E-04	3.875E-03	1.230E-02	2.472E-02	2.994E-02	1.481E-02	2.654E-05
TUD	−6.605E-07	5.260E-05	6.209E-04	3.853E-03	1.252E-02	2.528E-02	3.053E-02	1.502E-02	1.827E-05
Average	7.795E-08	6.936E-05	6.706E-04	3.909E-03	1.250E-02	2.515E-02	3.036E-02	1.495E-02	2.396E-05
Pronghorn	3.152E-07	6.751E-05	6.524E-04	3.836E-03	1.230E-02	2.478E-02	3.002E-02	1.488E-02	2.339E-05
Difference *%)	304.44	−2.68	−2.72	−1.86	−1.62	−1.45	−1.13	−0.52	−2.37

*Vertical velocity component in m/s.

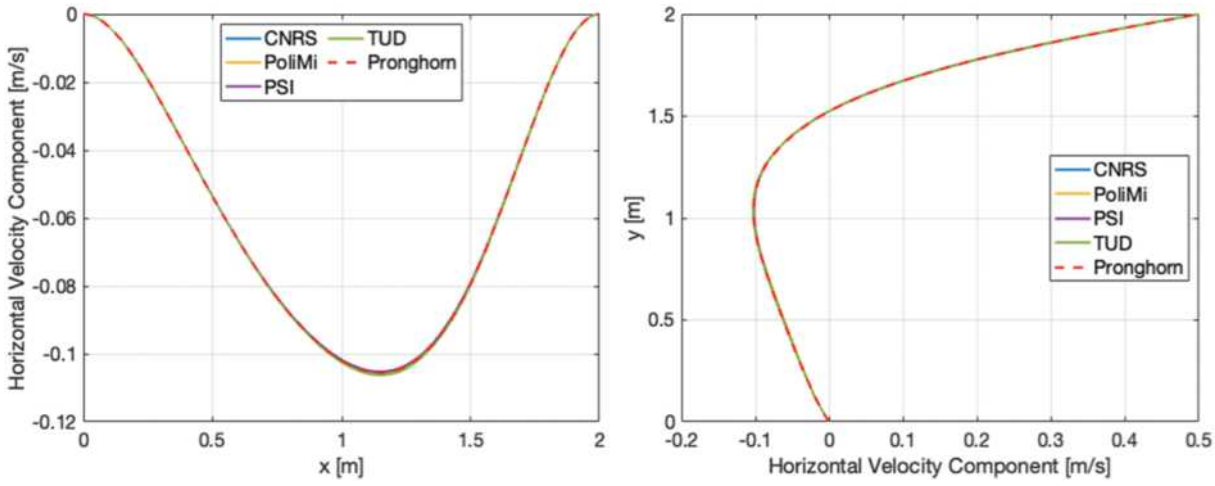

Fig. 3. Step 0.1—Horizontal velocity component distribution along (left) AA′ and (right) BB′.

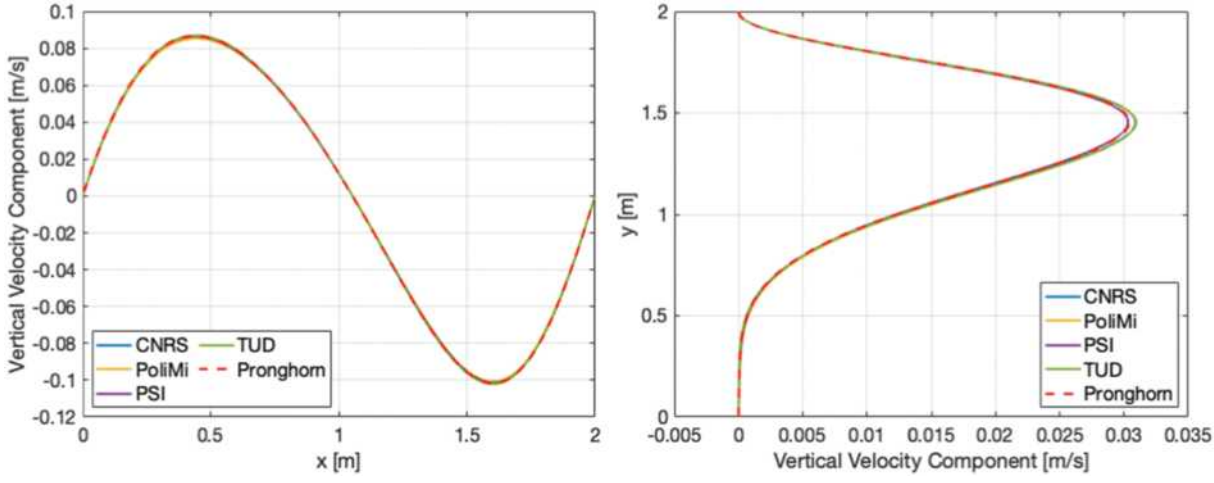

Fig. 4. Step 0.1—Vertical velocity component distribution along (left) AA′ and (right) BB′.

TABLE VII

Step 0.1—Average Discrepancies of Observable Field Quantities of Pronghorn and Reference Codes*

Observable		Average Discrepancy	
		Pronghorn	Reference Code
Horizontal velocity component	AA′	0.32	0.08 to 0.64
	BB′	0.23	0.35 to 0.68
Vertical velocity component	AA′	0.30	0.42 to 1.37
	BB′	1.24	0.50 to 1.96

*Average discrepancies in percent.

later sections, Pronghorn tends to dominate the computing time. For practicality, therefore, the 200 × 200 mesh is used in the subsequent calculations, as the overall solutions are still well captured by the coarse mesh.

III.A.2. Step 0.2: Neutronics

Tables VIII and IX compare the reactivity and the fission rate density at the selected points along line AA′, respectively, and Fig. 6 demonstrates the full fission rate

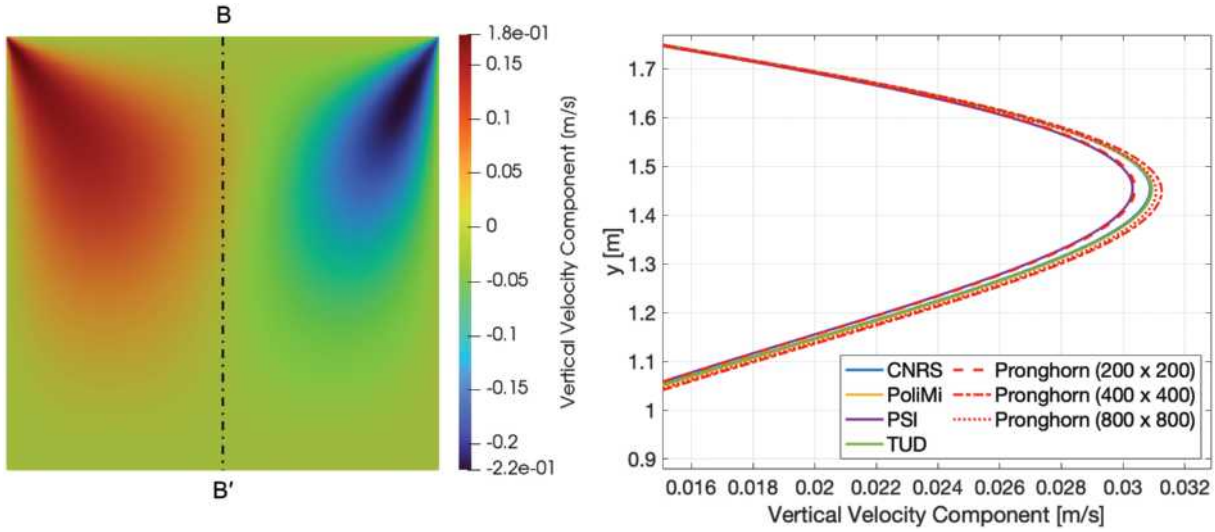

Fig. 5. Step 0.1—(left) Vertical velocity component field and (right) the effect of mesh refinement on the vertical velocity component along BB′ around the peak.

density distribution along AA′. The solutions along BB′ are omitted due to symmetry. The reactivity of Griffin is 22.6 pcm higher than the average. While this difference is within the standard deviation of 77.8 pcm, the large standard deviation is due to the scattered solutions coming from different angular discretization schemes (diffusion, SP3, SN) that affect reactivity sensitively by different boundary leakage treatments.

Thus, it is worthwhile to compare the reactivity of Griffin with the corresponding diffusion results (CNRS-SP1, PoliMi, and PSI); the differences are around 50 pcm. For the fission rate density, Griffin presents a cosine profile, as expected from a homogeneous medium, and yields the average discrepancy of 0.43%, which comes within the range of the reference codes' average discrepancies (0.10% to 0.65%), but the boundary values are overestimated by more than 8% compared to the reference codes.

TABLE VIII

Step 0.2—Reactivity

Code	ρ (pcm)
CNRS-SP1	411.3
CNRS-SP3	353.7
PoliMi	421.2
PSI	411.7
TUD-S2	482.6
TUD-S6	578.1
Average (standard deviation)	443.1 (77.8)
Griffin	465.7
Difference	22.6

In order to identify the source of discrepancies in the fission rate density at the boundaries and in the reactivity against diffusion results, a mesh refinement study was performed. The major difference between Griffin and the other diffusion codes stemmed from the use of FEM with a linear shape function, while the other codes are based on FVM, which basically corresponds to FEM with a piecewise constant shape function.

Thus, a convergence test with respect to the mesh refinement was performed with Griffin using a constant shape function, as presented in Table X. The reference is the current solution with the linear shape function and the 200 × 200 mesh. The Griffin solutions with the constant shape function intersect with the reference diffusion codes between the 200 × 200 and 400 × 400 mesh cases, but more mesh refinement above 1600 × 1600 is needed to obtain equivalent solutions with the linear shape function. To conclude, the discrepancies at the boundaries and in the reactivity are caused by the differences in the spatial discretization schemes. However, their effect is much less significant to the overall solutions and the reactivity "changes" that will be of interest in subsequent calculations, so the spatial under convergence of the reference codes is not considered a serious issue.

III.A.3. Step 0.3: Temperature

Table XI compares the temperature at the selected points along the centerlines, and Fig. 7 shows the full distributions along the centerlines. The largest discrepancies are seen at the boundaries, which is thought to be due

TABLE IX

Step 0.2—Fission Rate Density at Selected Points Along AA′*

Point (m)	0.01	0.25	0.5	0.75	1	1.25	1.5	1.75	1.99
Code	AA′								
CNRS-SP1	9.723E+17	7.436E+18	1.305E+19	1.678E+19	1.809E+19	1.678E+19	1.305E+19	7.436E+18	9.723E+17
CNRS-SP3	9.478E+17	7.450E+18	1.303E+19	1.673E+19	1.802E+19	1.673E+19	1.303E+19	7.450E+18	9.478E+17
PoliMi	9.902E+17	7.470E+18	1.310E+19	1.684E+19	1.815E+19	1.684E+19	1.310E+19	7.470E+18	9.902E+17
PSI	9.723E+17	7.436E+18	1.305E+19	1.678E+19	1.809E+19	1.678E+19	1.305E+19	7.436E+18	9.723E+17
TUD-S2	9.444E+17	7.433E+18	1.307E+19	1.682E+19	1.814E+19	1.682E+19	1.307E+19	7.433E+18	9.444E+17
TUD-S6	9.887E+17	7.463E+18	1.300E+19	1.667E+19	1.796E+19	1.667E+19	1.300E+19	7.463E+18	9.887E+17
Average	9.693E+17	7.448E+18	1.305E+19	1.677E+19	1.807E+19	1.677E+19	1.305E+19	7.448E+18	9.693E+17
Griffin	1.049E+18	7.451E+18	1.301E+19	1.670E+19	1.799E+19	1.670E+19	1.301E+19	7.451E+18	1.049E+18
Difference (%)	8.20	0.04	−0.32	−0.44	−0.48	−0.44	−0.32	0.04	8.20

*Fission rate density in $1/m^3/s$.

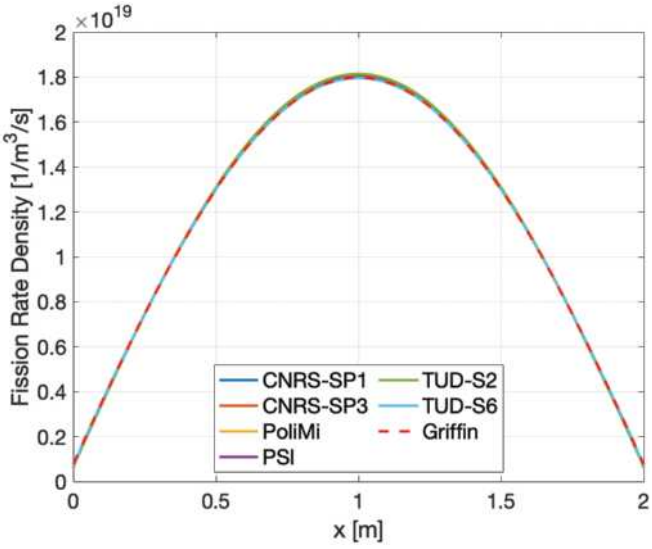

Fig. 6. Step 0.2—Fission rate density distribution along AA′.

to the fission rate density difference at the boundaries in step 0.2. But overall, Pronghorn yields the average discrepancies of only 0.09% along both centerlines, which are within the range of the reference codes' average discrepancies (0.05% to 0.14%).

III.B. Phase 1: Multiphysics Steady-State Benchmark

III.B.1. Step 1.1: Circulating Fuel

Tables XII and XIII report the comparison of the reactivity change from the static fuel case (step 0.2) and the delayed neutron source at the selected points along the centerlines, respectively, and Fig. 8 illustrates the full temperature distributions along the centerlines. Note that the delayed neutron source distribution is no longer symmetric, which shows the effect of the DNP drift.

Although the reference codes and Griffin presented scattered reactivities in the range of 350 to 580 pcm in step 0.2, the reactivity changes from those are closely gathered around −62 pcm. The reactivity change of Griffin differs by 0.7 pcm from the average, which is within the standard deviation of 0.8 pcm. However, when compared separately with the diffusion results, the reactivity change of Griffin is slightly smaller in magnitude, which is thought to be contributed by the reactivity differences in step 0.2.

For the delayed neutron source, the average discrepancies of Griffin turned out to be 0.57% along AA′ and 0.36% along BB′, which both fall within the range of the reference codes' average discrepancies (0.19% to 0.80% along AA′ and 0.16% to 0.72% along BB′). Relatively

TABLE X

Step 0.2—Griffin Solutions with Spatial Refinement Using Constant Shape Function

Mesh	Fission Rate Density (1/m^3/s)					Reactivity (pcm)
Point (m)	0.01	0.25	0.5	0.75	1	
200 × 200	9.222E+17	7.426E+18	1.308E+19	1.684E+19	1.815E+19	376.4
400 × 400	9.860E+17	7.439E+18	1.305E+19	1.677E+19	1.807E+19	421.3
800 × 800	1.017E+18	7.445E+18	1.303E+19	1.673E+19	1.803E+19	443.6
1600 × 1600	1.033E+18	7.448E+18	1.302E+19	1.671E+19	1.801E+19	454.8
Reference	1.049E+18	7.451E+18	1.301E+19	1.670E+19	1.799E+19	465.7

TABLE XI

Step 0.3—Temperature at Selected Points Along AA′ and BB′*

Point (m)	0.01	0.25	0.5	0.75	1	1.25	1.5	1.75	1.99
Code	AA′								
CNRS-SP1	931.78	1193.92	1358.39	1362.68	1304.93	1224.38	1131.12	1033.74	930.99
CNRS-SP3	931.01	1193.98	1357.29	1361.49	1304.13	1224.09	1131.34	1034.34	930.15
PoliMi	932.30	1195.54	1360.54	1363.83	1305.17	1224.44	1131.68	1034.52	931.61
PSI	931.92	1195.92	1356.02	1362.62	1305.83	1225.64	1133.03	1036.93	931.15
TUD-S2	930.97	1193.96	1358.92	1363.52	1305.47	1224.44	1130.94	1032.07	929.87
TUD-S6	932.45	1193.89	1355.76	1360.13	1303.11	1223.47	1131.37	1033.75	931.25
Average	931.74	1194.54	1357.82	1362.38	1304.77	1224.41	1131.58	1034.23	930.84
Griffin	934.28	1193.76	1356.50	1360.68	1303.52	1223.76	1131.30	1034.72	933.39
Difference (%)	0.27	−0.06	−0.10	−0.12	−0.10	−0.05	−0.02	0.05	0.27
Code	BB′								
CNRS-SP1	931.51	1139.47	1272.84	1304.79	1304.93	1314.09	1321.05	1264.97	971.06
CNRS-SP3	930.72	1139.87	1272.32	1303.97	1304.13	1313.30	1320.27	1264.53	971.43
PoliMi	932.07	1140.37	1274.95	1306.62	1305.17	1313.41	1320.66	1265.23	973.77
PSI	931.51	1139.14	1273.01	1306.69	1305.83	1312.01	1319.21	1262.75	977.34
TUD-S2	930.64	1139.42	1273.23	1305.50	1305.47	1314.81	1321.66	1265.14	970.93
TUD-S6	932.08	1140.29	1271.63	1303.12	1303.11	1312.47	1319.32	1263.75	972.50
Average	931.42	1139.76	1273.00	1305.12	1304.77	1313.35	1320.36	1264.40	972.84
Griffin	933.96	1139.88	1271.83	1303.34	1303.52	1312.70	1319.67	1264.10	970.26
Difference (%)	0.27	0.01	−0.09	−0.14	−0.10	−0.05	−0.05	−0.02	−0.27

*Temperature in kelvins.

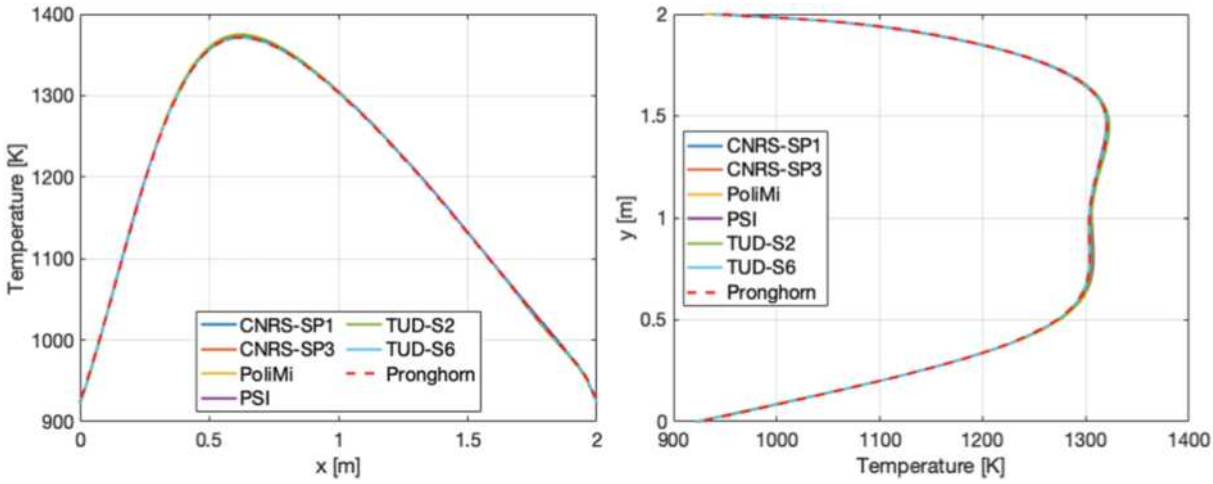

Fig. 7. Step 0.3—Temperature distribution along (left) AA′ and (right) BB′.

TABLE XII

Step 1.1—Reactivity Change from Step 0.2

Code	$P - \rho_{0.2}$ (pcm)
CNRS-SP1	−62.5
CNRS-SP3	−62.6
PoliMi	−62.0
PSI	−63.0
TUD-S2	−62.0
TUD-S6	−60.7
Average (standard deviation)	−62.1 (0.8)
Griffin	−61.4
Difference	0.7

large discrepancies of over 9% are observed at the boundaries, but they are thought to be originating from the difference in the fission rate density in step 0.2, as the amount of delayed neutron source is directly proportional to the fission rate density.

To reiterate, the differences in step 0.2 are due to the fact that Griffin is utilizing the linear FEM in lieu of FVM and that a linear shape function has better spatial convergence than a constant shape function. Considering the reactivity change and the delayed neutron source, therefore, it can be deduced that the DNP drift is being simulated correctly in the Griffin-Pronghorn code system, and the discrepancies at the boundaries are due to the differences in the baseline neutronics solutions caused by the different discretization schemes.

III.B.2. Step 1.2: Power Coupling

Table XIV presents the reactivity change from the constant temperature case (step 1.1), and Tables XV and XVI compare the temperature and the change of fission rate density from step 0.2 at the selected points along the centerlines, respectively. Their full distributions along the centerlines are illustrated in Figs. 9 and 10. The Griffin solutions present expected behaviors from a physics point of view. Coupling in the power and temperature should result in a negative reactivity insertion, which is expected, and the fission rate density should increase in the peripheries and decrease at the center region where higher temperatures are observed, as the center region sees stronger negative feedback than the peripheries while the power level is constant.

Griffin yields the reactivity change, which is off by −1.3 pcm from the average. It falls within the standard deviation of 13.7 pcm, but similarly to step 1.1, its magnitude is slightly smaller compared to the diffusion results, likely due to the same cause. The average discrepancies of the temperature and fission rate density change are also presented in Table XVII. The fission rate density change reported by TUD presents a sawtooth shape due to its discretization scheme, which makes the average discrepancies of fission rate density change relatively larger. However, the average discrepancies of Griffin are still within the range.

It is also worth reiterating that the relatively large discrepancies of both temperature and fission rate density change near the boundaries are normal, as it is already known that all the downstream results are affected by the differences in the baseline neutronics solutions which are originating from the different discretization schemes.

III.B.3. Step 1.3: Buoyancy

Table XVIII compares the reactivity change from step 0.2, and the observable field quantities are compared at the

TABLE XIII

Step 1.1—Delayed Neutron Source at Selected Points Along AA′ and BB′*

Point (m)	0.01	0.25	0.5	0.75	1	1.25	1.5	1.75	1.99
Code	AA′								
CNRS-SP1	1.687E+16	1.452E+17	2.212E+17	2.411E+17	2.268E+17	1.923E+17	1.461E+17	9.214E+16	1.693E+16
CNRS-SP3	1.651E+16	1.454E+17	2.209E+17	2.406E+17	2.264E+17	1.921E+17	1.462E+17	9.245E+16	1.653E+16
PoliMi	1.701E+16	1.450E+17	2.219E+17	2.414E+17	2.266E+17	1.920E+17	1.459E+17	9.188E+16	1.688E+16
PSI	1.684E+16	1.453E+17	2.214E+17	2.413E+17	2.270E+17	1.925E+17	1.463E+17	9.218E+16	1.760E+16
TUD-S2	1.619E+16	1.438E+17	2.228E+17	2.426E+17	2.278E+17	1.927E+17	1.464E+17	8.968E+16	1.650E+16
TUD-S6	1.695E+16	1.437E+17	2.212E+17	2.405E+17	2.261E+17	1.916E+17	1.461E+17	9.029E+16	1.718E+16
Average	1.673E+16	1.447E+17	2.216E+17	2.413E+17	2.268E+17	1.922E+17	1.462E+17	9.144E+16	1.694E+16
Griffin	1.831E+16	1.452E+17	2.207E+17	2.407E+17	2.263E+17	1.919E+17	1.458E+17	9.241E+16	1.851E+16
Difference (%)	9.44	0.28	−0.37	−0.25	−0.23	−0.18	−0.24	1.07	9.27
Code	BB′								
CNRS-SP1	1.626E+16	1.190E+17	1.881E+17	2.193E+17	2.268E+17	2.261E+17	2.178E+17	1.754E+17	4.526E+16
CNRS-SP3	1.586E+16	1.193E+17	1.879E+17	2.189E+17	2.264E+17	2.257E+17	2.175E+17	1.753E+17	4.534E+16
PoliMi	1.647E+16	1.186E+17	1.881E+17	2.194E+17	2.266E+17	2.260E+17	2.177E+17	1.756E+17	4.538E+16
PSI	1.624E+16	1.189E+17	1.881E+17	2.195E+17	2.270E+17	2.261E+17	2.176E+17	1.752E+17	4.447E+16
TUD-S2	1.576E+16	1.174E+17	1.882E+17	2.203E+17	2.278E+17	2.281E+17	2.193E+17	1.768E+17	4.169E+16
TUD-S6	1.648E+16	1.178E+17	1.872E+17	2.186E+17	2.261E+17	2.264E+17	2.179E+17	1.761E+17	4.240E+16
Average	1.618E+16	1.185E+17	1.879E+17	2.193E+17	2.268E+17	2.264E+17	2.180E+17	1.757E+17	4.409E+16
Griffin	1.755E+16	1.195E+17	1.876E+17	2.186E+17	2.263E+17	2.257E+17	2.174E+17	1.752E+17	4.625E+16
Difference (%)	8.48	0.83	−0.15	−0.31	−0.23	−0.31	−0.27	−0.32	4.91

*Delayed neutron source in $1/m^3/s$.

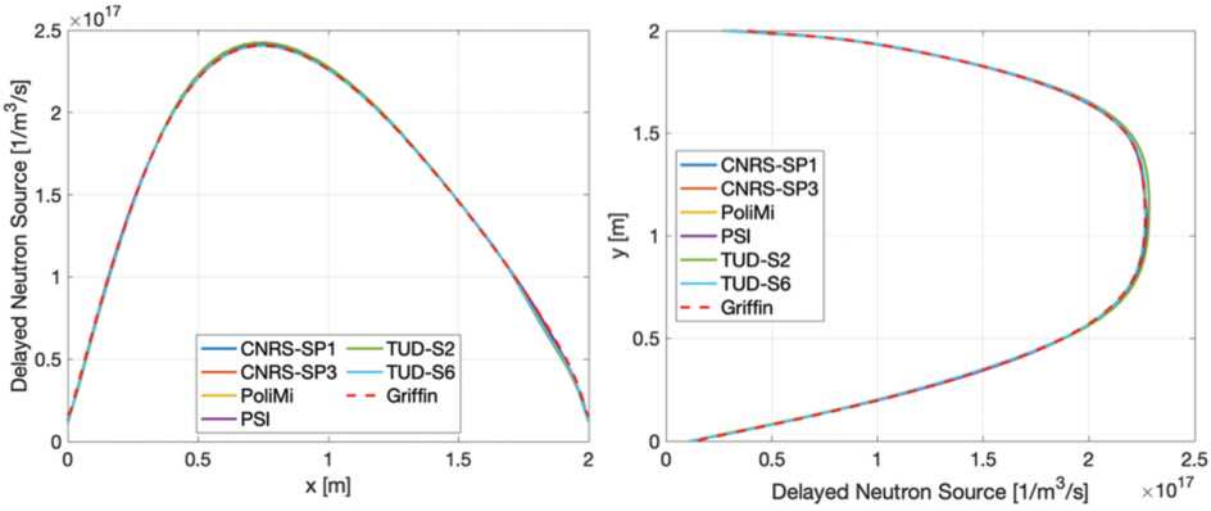

Fig. 8. Step 1.1—Delayed neutron source distribution along (left) AA′ and (right) BB′.

TABLE XIV

Step 1.2—Reactivity Change from Step 1.1

Code	$\rho - \rho_{1.1}$ (pcm)
CNRS-SP1	−1152.0
CNRS-SP3	−1152.7
PoliMi	−1161.0
PSI	−1154.8
TUD-S2	−1145.2
TUD-S6	−1122.0
Average (standard deviation)	−1148.0 (13.7)
Griffin	−1149.3
Difference	−1.3

selected points along the centerlines throughout Tables XIX through XXII and illustrated throughout Figs. 11 through 14. The average discrepancies are also reported in Table XXIII. The flow field by buoyancy forms two large axisymmetric eddies with respect to BB′, and as a result, the horizontal velocity component is zero everywhere along BB′. Thus, it is not presented.

All the field quantities present either symmetric or antisymmetric distributions along AA′ and tend to skew toward the top along BB′, which is an expected behavior and an indication that the natural convection by buoyancy is properly modeled. The large difference at the center of AA′ in the horizontal velocity component is meaningless because it is occurring at the point of antisymmetry. Namely, in the absence of numerical errors, the horizontal velocity component should be zero at that particular point.

Similar to the earlier steps, the reactivity change of Griffin is within the standard deviation but tends to be smaller in magnitude compared to the diffusion results. Most of the field quantities show good agreements with the reference codes, given that the relatively large discrepancies at the boundaries are expected results. However, some quantities present average discrepancies that go above the range of the reference codes' average discrepancies, which are the temperature along both centerlines and the delayed neutron source along AA′.

In the case of the delayed neutron source, it tends to be underestimated compared to the reference codes together with the horizontal velocity component along AA′. The underestimation of the horizontal velocity component can be interpreted as there is less inflow of fuel and DNPs toward the center, which leads to reduced DNPs in the center. The reason for the underestimation has not been examined thoroughly, but the mesh discretization issue discussed in step 0.1 is suspected. The reduction of delayed neutron source in the center region in turn results in less power, which can contribute to the underestimation of the temperature to some extent. For further investigation, however, the fission rate density itself will have to be compared, which was not provided by the benchmark.

III.B.4. Step 1.4: Full Coupling

Table XXIV compares the reactivity change with respect to step 0.2 for each combination of lid velocity and power. Higher power leads to larger negative reactivity insertion, which is expected by the reduction of fuel salt density, and the different impacts of the lid velocity on the reactivity, depending on the power caused by the mixed effect of energy and DNP redistribution (higher lid velocity tends to reduce the reactivity for lower power and increase the reactivity for

TABLE XV

Step 1.2—Temperature at Selected Points Along AA′ and BB′*

Point (m)	0.01	0.25	0.5	0.75	1	1.25	1.5	1.75	1.99
Code	AA′								
CNRS-SP1	935.08	1195.02	1341.29	1348.64	1298.48	1224.75	1136.33	1041.40	934.23
CNRS-SP3	934.26	1195.27	1340.60	1347.63	1297.87	1224.65	1136.64	1042.28	933.32
PoliMi	935.83	1197.76	1343.29	1350.18	1299.64	1225.99	1138.09	1044.57	935.08
PSI	935.41	1197.28	1340.30	1349.10	1300.18	1226.98	1139.02	1045.23	934.54
TUD-S2	934.25	1195.75	1342.97	1350.19	1300.05	1225.90	1136.88	1040.67	933.03
TUD-S6	935.84	1195.54	1339.95	1346.87	1297.62	1224.78	1137.19	1042.33	934.50
Average	935.11	1196.10	1341.40	1348.77	1298.97	1225.51	1137.36	1042.75	934.12
Griffin	937.96	1195.47	1340.59	1347.40	1298.01	1225.07	1137.13	1043.36	936.97
Difference (%)	0.30	−0.05	−0.06	−0.10	−0.07	−0.04	−0.02	0.06	0.31
Code	BB′								
CNRS-SP1	934.98	1148.24	1266.85	1300.49	1298.60	1303.13	1307.73	1261.57	974.91
CNRS-SP3	934.12	1148.73	1266.60	1299.91	1297.96	1302.68	1307.27	1261.34	975.48
PoliMi	935.62	1149.58	1269.69	1303.29	1299.89	1302.88	1308.04	1262.14	981.76
PSI	935.13	1148.37	1267.67	1302.68	1300.45	1302.51	1307.16	1260.49	981.28
TUD-S2	934.05	1148.49	1269.10	1301.82	1300.18	1304.80	1309.33	1263.11	975.10
TUD-S6	935.59	1149.11	1267.35	1299.30	1297.73	1302.46	1307.07	1261.72	976.75
Average	934.92	1148.75	1267.88	1301.25	1299.14	1303.08	1307.77	1261.73	977.55
Griffin	937.82	1149.00	1272.33	1300.01	1298.01	1303.57	1306.62	1253.00	974.71
Difference (%)	0.31	0.02	0.35	−0.09	−0.09	0.04	−0.09	−0.69	−0.29

*Temperature in kelvins.

TABLE XVI

Step 1.2—Fission Rate Density Change from Step 0.2 at Selected Points Along AA′ and BB′*

Point (m)	0.01	0.25	0.5	0.75	1	1.25	1.5	1.75	1.99
Code	AA′								
CNRS-SP1	1.060E+17	1.169E+17	−5.694E+17	−9.490E+17	−7.979E+17	−2.853E+17	2.626E+17	4.611E+17	1.059E+17
CNRS-SP3	1.029E+17	1.156E+17	−5.668E+17	−9.427E+17	−7.941E+17	−2.869E+17	2.575E+17	4.578E+17	1.027E+17
PoliMi	1.037E+17	1.141E+17	−5.682E+17	−9.440E+17	−7.906E+17	−2.800E+17	2.628E+17	4.563E+17	1.034E+17
PSI	1.076E+17	1.226E+17	−5.486E+17	−9.275E+17	−7.807E+17	−2.725E+17	2.702E+17	4.632E+17	1.074E+17
TUD-S2	9.974E+16	1.069E+17	−5.648E+17	−9.534E+17	−8.186E+17	−2.724E+17	2.628E+17	4.531E+17	9.995E+16
TUD-S6	1.028E+17	1.041E+17	−5.572E+17	−9.382E+17	−8.098E+17	−2.791E+17	2.466E+17	4.431E+17	1.027E+17
Average	1.038E+17	1.134E+17	−5.625E+17	−9.425E+17	−7.986E+17	−2.794E+17	2.604E+17	4.558E+17	1.037E+17
Griffin	1.143E+17	1.206E+17	−5.620E+17	−9.405E+17	−7.963E+17	−2.936E+17	2.492E+17	4.514E+17	1.120E+17
Difference (%)	10.12	6.38	−0.09	−0.21	−0.28	5.10	−4.32	−0.97	7.97
Code	BB′								
CNRS-SP1	1.117E+17	2.640E+17	−2.264E+17	−6.431E+17	−7.979E+17	−7.557E+17	−4.923E+17	−3.953E+16	1.046E+17
CNRS-SP3	1.084E+17	2.615E+17	−2.273E+17	−6.407E+17	−7.941E+17	−7.525E+17	−4.902E+17	−3.919E+16	1.009E+17
PoliMi	1.095E+17	2.639E+17	−2.256E+17	−6.389E+17	−7.942E+17	−7.536E+17	−4.922E+17	−4.164E+16	1.013E+17
PSI	1.118E+17	2.639E+17	−2.287E+17	−6.506E+17	−8.020E+17	−7.479E+17	−4.856E+17	−3.479E+16	1.033E+17
TUD-S2	1.053E+17	2.513E+17	−2.336E+17	−6.589E+17	−8.186E+17	−7.703E+17	−4.964E+17	−4.656E+16	9.186E+16
TUD-S6	1.082E+17	2.436E+17	−2.373E+17	−6.540E+17	−8.098E+17	−7.612E+17	−4.906E+17	−4.534E+16	9.449E+16
Average	1.091E+17	2.580E+17	−2.298E+17	−6.477E+17	−8.028E+17	−7.569E+17	−4.912E+17	−4.118E+16	9.941E+16
Griffin	1.205E+17	2.640E+17	−2.297E+17	−6.420E+17	−7.917E+17	−7.457E+17	−4.849E+17	−4.146E+16	1.066E+17
Difference (%)	10.40	2.33	−0.06	−0.88	−1.38	−1.48	−1.28	0.69	7.20

*Fission rate density change in $1/m^3/s$.

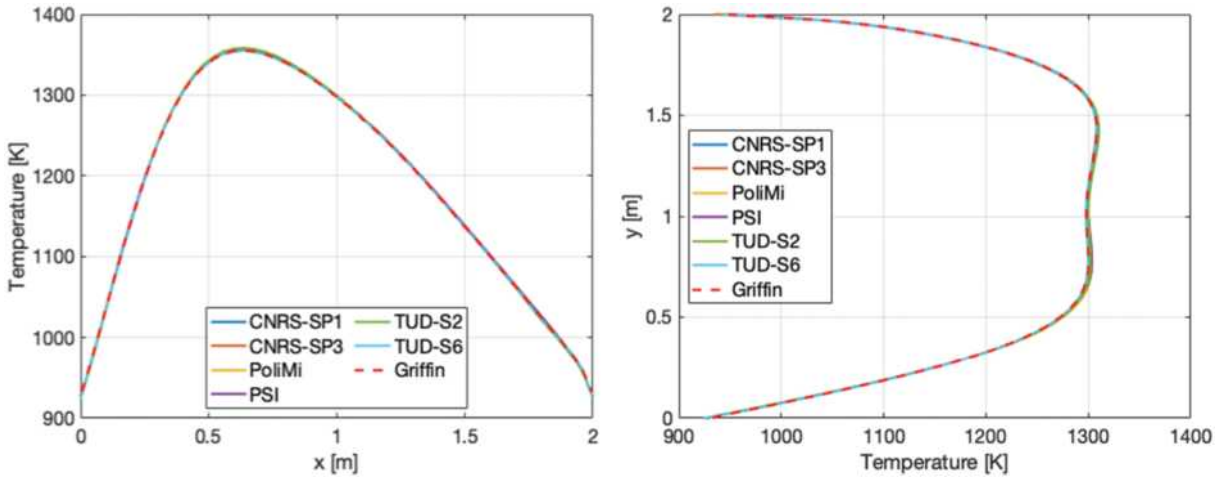

Fig. 9. Step 1.2—Temperature distribution along (left) AA′ and (right) BB′.

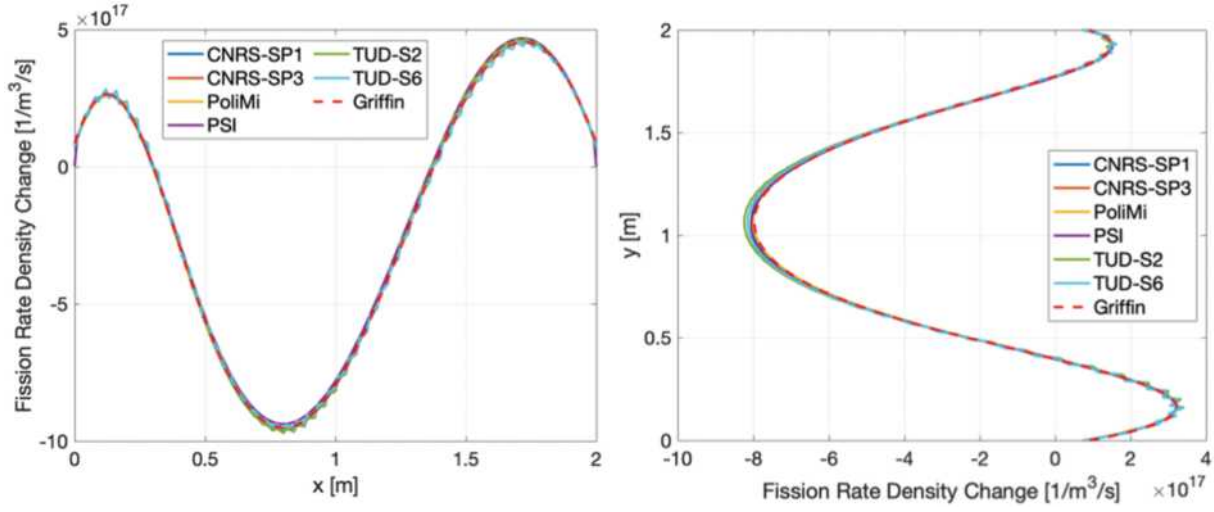

Fig. 10. Step 1.2—Fission rate density change distribution from step 0.2 along (left) AA′ and (right) BB′.

TABLE XVII

Step 1.2—Average Discrepancies of Observable Field Quantities of Griffin and Reference Codes*

Observable		Average Discrepancy	
		Griffin	Reference Codes
Temperature	AA′	0.08	0.09 to 0.13
	BB′	0.08	0.06 to 0.12
Fission rate density change	AA′	1.19	1.03 to 2.59
	BB′	1.35	0.80 to 2.33

*Average discrepancies in percent.

TABLE XVIII

Step 1.3—Reactivity Change from Step 0.2

Code	$\rho - \rho_{0.2}$ (pcm)
CNRS-SP1	−1220.5
CNRS-SP3	−1220.7
PoliMi	−1227.0
PSI	−1219.6
TUD-S2	−1208.5
TUD-S6	−1184.4
Average (standard deviation)	−1213.5 (15.4)
Griffin	−1212.0
Difference	1.5

higher power) is also captured properly. The differences in reactivity changes against the averages do not exceed ±2.5 pcm and fall within the standard deviations in all cases.

Table XXV reports the number of Picard iterations and the run times of Griffin and Pronghorn for each case using 48 CPU cores on the INL Sawtooth cluster. The Picard iteration was terminated when the relative reduction of Griffin's flux residual reached 10^{-5}. The convergence tends to worsen with higher power and lid velocity. Nevertheless, the Picard iterations converge quickly within three to five iterations for all cases.

The run time is dominated by Pronghorn; over 97% of the total run time is consumed by Pronghorn in every case. This is because Pronghorn currently does not have a steady-state calculation option and should always perform time marching until steady state is reached. Namely, Pronghorn solves a transient problem at each Picard iteration, which makes Pronghorn significantly more expensive than Griffin. This can be potentially improved in the future by implementing dedicated algorithms for steady flow calculations in Pronghorn, such as the Semi-Implicit Method for Pressure-Linked Equations or SIMPLE[48] algorithm or its variants.

Figure 15 illustrates the flow speed and DNP density distributions depending on the lid velocity for the 1.0-GW power case, which is a qualitative verification of the fully coupled DNP drift simulation. The degree of DNP dispersion depends on their half-lives; the first-group DNPs, which have the longest half-life, are largely dispersed following the fluid as they can last long enough to be carried away by the fluid. The latter-group of DNPs are more centered at the cavity following the fission rate distribution due to their shorter half-lives. The impact of forced convection on the DNP distributions can also be observed, especially in the first-group DNPs.

To conclude, all the steady-state multiphysics phenomena expected in a flowing-fuel MSR are well

TABLE XIX

Step 1.3—Horizontal Velocity Component at Selected Points Along AA′*

Point (m)	AA′								
Code	0.01	0.25	0.5	0.75	1	1.25	1.5	1.75	1.99
CNRS-SP1	8.061E-05	1.641E-02	2.310E-02	8.061E-05	1.250E-09	−1.579E-02	−2.310E-02	−1.641E-02	−8.061E-05
CNRS-SP3	8.023E-05	1.636E-02	2.302E-02	1.572E-02	1.000E-09	−1.572E-02	−2.302E-02	−1.636E-02	−8.023E-05
PoliMi	7.334E-05	1.637E-02	2.312E-02	1.578E-02	−1.125E-10	−1.578E-02	−2.312E-02	−1.637E-02	−7.334E-05
PSI	8.012E-05	1.630E-02	2.263E-02	1.519E-02	−8.525E-09	−1.519E-02	−2.263E-02	−1.630E-02	−8.012E-05
TUD-S2	7.684E-05	1.644E-02	2.316E-02	1.584E-02	−2.218E-06	−1.584E-02	−2.316E-02	−1.644E-02	−7.684E-05
TUD-S6	7.614E-05	1.631E-02	2.295E-02	1.566E-02	−2.196E-06	−1.566E-02	−2.295E-02	−1.631E-02	−7.614E-05
Average	7.788E-05	1.636E-02	2.300E-02	1.566E-02	−7.366E-07	−1.566E-02	−2.300E-02	−1.636E-02	−7.788E-05
Griffin	7.568E-05	1.640E-02	2.269E-02	1.518E-02	−1.937E-13	−1.518E-02	−2.269E-02	−1.640E-02	−7.568E-05
Difference (%)	−2.82	0.22	−1.32	−3.07	−100.00	−3.07	−1.32	0.22	−2.82

*Horizontal velocity component in m/s.

TABLE XX

Step 1.3—Vertical Velocity Component at Selected Points Along AA′ and BB′*

Point (m)	0.01	0.25	0.5	0.75	1	1.25	1.5	1.75	1.99
Code	AA′								
CNRS-SP1	−2.836E-02	−1.777E-01	1.721E-02	1.376E-01	1.649E-01	1.376E-01	1.721E-02	−1.777E-01	−2.836E-02
CNRS-SP3	−2.828E-02	−1.771E-01	1.708E-02	1.372E-01	1.645E-01	1.372E-01	1.708E-02	−1.771E-01	−2.828E-02
PoliMi	−2.837E-02	−1.767E-01	1.741E-02	1.368E-01	1.638E-01	1.368E-01	1.741E-02	−1.767E-01	−2.837E-02
PSI	−2.820E-02	−1.779E-01	1.662E-02	1.376E-01	1.659E-01	1.376E-01	1.662E-02	−1.779E-01	−2.820E-02
TUD-S2	−2.846E-02	−1.780E-01	1.735E-02	1.379E-01	1.650E-01	1.379E-01	1.735E-02	−1.780E-01	−2.846E-02
TUD-S6	−2.817E-02	−1.766E-01	1.694E-02	1.368E-01	1.639E-01	1.368E-01	1.694E-02	−1.766E-01	−2.817E-02
Avg.	−2.831E-02	−1.773E-01	1.710E-02	1.373E-01	1.647E-01	1.373E-01	1.710E-02	−1.773E-01	−2.831E-02
Griffin	−2.804E-02	−1.772E-01	1.644E-02	1.371E-01	1.652E-01	1.371E-01	1.644E-02	−1.772E-01	−2.804E-02
Difference (%)	−0.95	−0.09	−3.86	−0.19	0.32	−0.19	−3.86	−0.09	−0.95
Code	BB′								
CNRS-SP1	1.008E-04	3.512E-02	8.947E-02	1.359E-01	1.649E-01	1.665E-01	1.307E-01	5.756E-02	1.710E-04
CNRS-SP3	1.009E-04	3.510E-02	8.933E-02	1.356E-01	1.645E-01	1.660E-01	1.303E-01	5.740E-02	1.704E-04
PoliMi	9.217E-05	3.507E-02	8.909E-02	1.351E-01	1.638E-01	1.656E-01	1.302E-01	5.743E-02	1.558E-04
PSI	1.019E-04	3.537E-02	9.055E-02	1.374E-01	1.659E-01	1.669E-01	1.309E-01	5.780E-02	1.729E-04
TUD-S2	9.089E-05	3.510E-02	8.950E-02	1.360E-01	1.650E-01	1.667E-01	1.308E-01	5.763E-02	1.496E-04
TUD-S6	9.109E-05	3.506E-02	8.912E-02	1.352E-01	1.639E-01	1.655E-01	1.299E-01	5.719E-02	1.481E-04
Average	9.630E-05	3.514E-02	8.951E-02	1.359E-01	1.647E-01	1.662E-01	1.305E-01	5.750E-02	1.613E-04
Griffin	9.119E-05	3.545E-02	9.041E-02	1.369E-01	1.652E-01	1.662E-01	1.304E-01	5.758E-02	1.503E-04
Difference (%)	−5.30	0.89	1.00	0.73	0.32	0.03	−0.02	0.14	−6.81

*Vertical velocity component in m/s.

TABLE XXI

Step 1.3—Temperature at Selected Points along AA′ and BB′*

Point (m)	0.01	0.25	0.5	0.75	1	1.25	1.5	1.75	1.99
Code	AA′								
CNRS-SP1	932.52	1192.71	1278.30	1284.47	1280.05	1284.47	1278.30	1192.71	932.52
CNRS-SP3	931.67	1192.52	1277.83	1284.04	1279.63	1284.04	1277.83	1192.52	931.67
PoliMi	933.12	1193.39	1279.11	1285.72	1281.69	1285.72	1279.11	1193.39	933.12
PSI	932.77	1190.97	1278.04	1284.03	1279.54	1284.03	1278.04	1190.97	932.77
TUD-S2	931.63	1193.15	1278.72	1284.82	1280.93	1284.82	1278.72	1193.15	931.63
TUD-S6	933.11	1192.38	1277.21	1283.44	1279.59	1283.44	1277.21	1192.38	933.11
Average	932.47	1192.52	1278.20	1284.42	1280.24	1284.42	1278.20	1192.52	932.47
Griffin	935.46	1190.35	1276.98	1282.85	1278.48	1282.85	1276.98	1190.35	935.46
Difference (%)	0.32	−0.18	−0.10	−0.12	−0.14	−0.12	−0.10	−0.18	0.32
Code	BB′								
CNRS-SP1	934.42	1066.51	1155.68	1226.24	1280.05	1315.32	1325.87	1283.01	937.10
CNRS-SP3	933.45	1067.36	1156.01	1226.15	1279.63	1314.70	1325.15	1282.44	936.32
PoliMi	934.95	1067.26	1156.78	1227.67	1281.69	1317.03	1327.46	1284.40	937.18
PSI	934.69	1067.51	1156.15	1226.16	1279.54	1314.18	1324.24	1281.45	938.77
TUD-S2	933.33	1066.43	1156.10	1226.94	1280.93	1316.26	1326.70	1283.45	935.51
TUD-S6	934.81	1068.65	1156.81	1226.48	1279.59	1314.33	1324.52	1281.71	937.25
Average	934.27	1067.29	1156.26	1226.61	1280.24	1315.30	1325.66	1282.74	937.02
Griffin	937.44	1068.99	1156.47	1225.62	1278.48	1313.14	1323.17	1280.33	943.02
Difference (%)	0.34	0.16	0.02	−0.08	−0.14	−0.16	−0.19	−0.19	0.64

*Temperature in kelvins.

TABLE XXII

Step 1.3—Delayed Neutron Source at Selected Points Along AA′ and BB′*

Point (m)	0.01	0.25	0.5	0.75	1	1.25	1.5	1.75	1.99
Code	AA′								
CNRS-SP1	2.014E+16	1.468E+17	2.001E+17	2.123E+17	1.988E+17	2.123E+17	2.001E+17	1.468E+17	2.014E+16
CNRS-SP3	1.974E+16	1.469E+17	2.000E+17	2.121E+17	1.986E+17	2.121E+17	2.000E+17	1.469E+17	1.974E+16
PoliMi	1.938E+16	1.464E+17	1.992E+17	2.113E+17	1.944E+17	2.113E+17	1.992E+17	1.464E+17	1.938E+16
PSI	2.003E+16	1.469E+17	2.005E+17	2.126E+17	1.983E+17	2.126E+17	2.005E+17	1.469E+17	2.003E+16
TUD-S2	1.787E+16	1.488E+17	2.017E+17	2.141E+17	1.942E+17	2.141E+17	2.017E+17	1.488E+17	1.787E+16
TUD-S6	1.859E+16	1.485E+17	2.006E+17	2.128E+17	1.931E+17	2.128E+17	2.006E+17	1.485E+17	1.859E+16
Average	1.929E+16	1.474E+17	2.003E+17	2.125E+17	1.962E+17	2.125E+17	2.003E+17	1.474E+17	1.929E+16
Griffin	2.165E+16	1.453E+17	1.980E+17	2.098E+17	1.949E+17	2.098E+17	1.980E+17	1.453E+17	2.165E+16
Difference (%)	12.21	−1.43	−1.15	−1.26	−0.67	−1.26	−1.15	−1.43	12.21
Code	BB′								
CNRS-SP1	1.808E+16	8.797E+16	1.377E+17	1.746E+17	1.988E+17	2.087E+17	2.017E+17	1.659E+17	2.620E+16
CNRS-SP3	1.758E+16	8.839E+16	1.378E+17	1.746E+17	1.986E+17	2.084E+17	2.015E+17	1.659E+17	2.584E+16
PoliMi	1.813E+16	8.624E+16	1.344E+17	1.706E+17	1.944E+17	2.045E+17	1.977E+17	1.623E+17	2.516E+16
PSI	1.811E+16	8.782E+16	1.373E+17	1.741E+17	1.983E+17	2.083E+17	2.014E+17	1.658E+17	2.612E+16
TUD-S2	1.738E+16	8.510E+16	1.335E+17	1.700E+17	1.942E+17	2.047E+17	1.980E+17	1.621E+17	2.361E+16
TUD-S6	1.812E+16	8.605E+16	1.335E+17	1.693E+17	1.931E+17	2.034E+17	1.969E+17	1.616E+17	2.444E+16
Average	1.790E+16	8.693E+16	1.357E+17	1.722E+17	1.962E+17	2.063E+17	1.995E+17	1.639E+17	2.523E+16
Griffin	1.933E+16	8.746E+16	1.354E+17	1.713E+17	1.949E+17	2.049E+17	1.982E+17	1.631E+17	2.783E+16
Difference (%)	8.02	0.61	−0.20	−0.54	−0.67	−0.69	−0.67	−0.49	10.31

*Delayed neutron source in $1/m^3/s$.

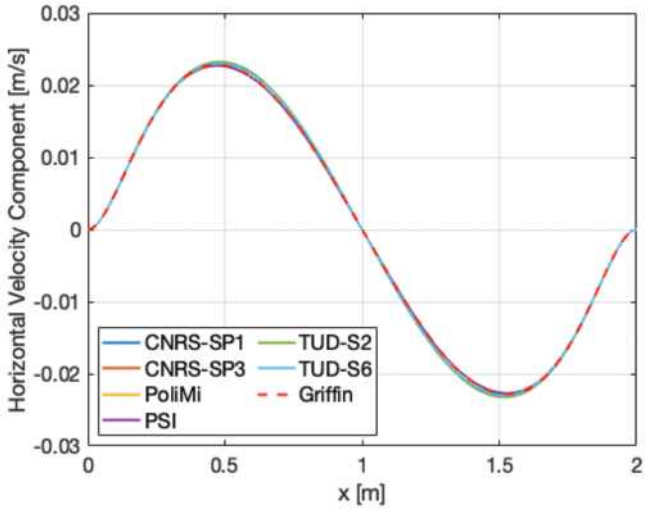

Fig. 11. Step 1.3—Horizontal velocity component distribution along AA′.

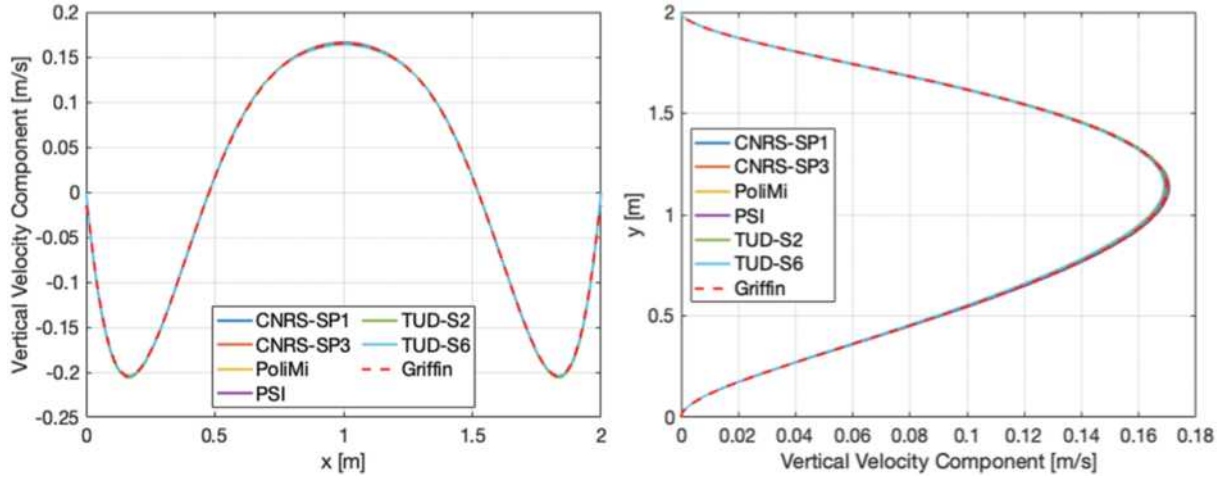

Fig. 12. Step 1.3—Vertical velocity component distribution along (left) AA′ and (right) BB′.

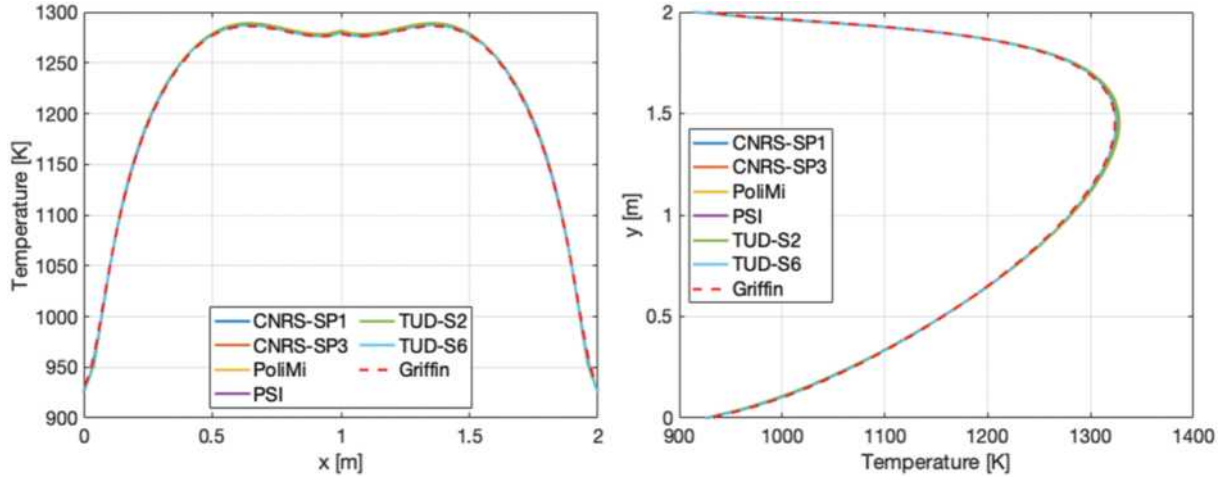

Fig. 13. Step 1.3—Temperature distribution along (left) AA′ and (right) BB′.

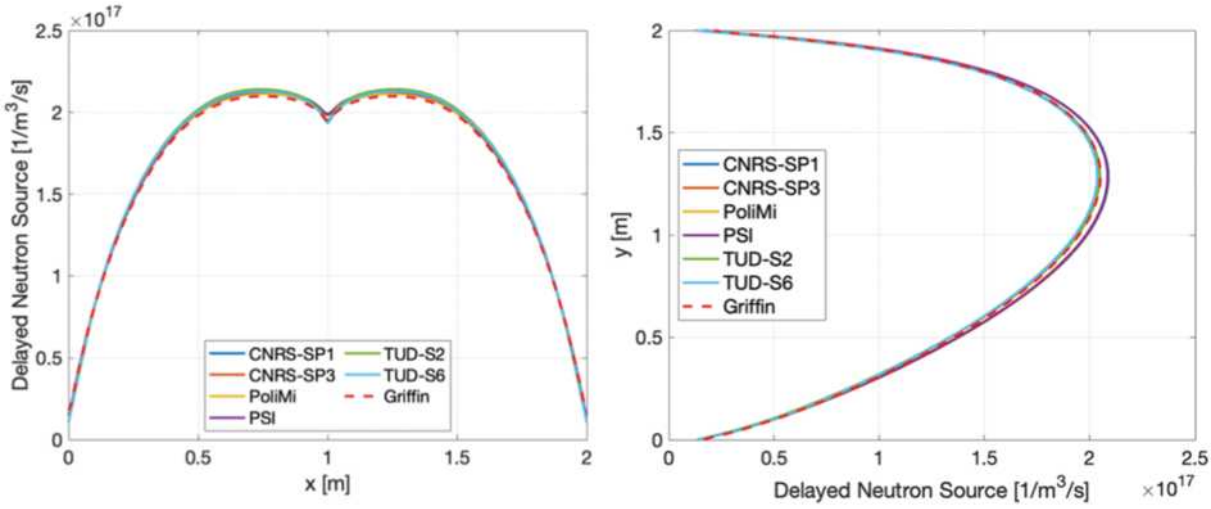

Fig. 14. Step 1.3—Delayed neutron source distribution along (left) AA′ and (right) BB′.

TABLE XXIII

Step 1.3—Average Discrepancies of Observable Field Quantities of Griffin and Reference Codes*

Observable		Average Discrepancy	
		Griffin	Reference Codes
Horizontal velocity component	AA′	1.78	0.23 to 2.24
Vertical velocity component	AA′	0.46	0.24 to 0.55
	BB′	0.46	0.16 to 0.89
Temperature	AA′	0.16	0.03 to 0.10
	BB′	0.18	0.05 to 0.10
Delayed neutron source	AA′	1.25	0.25 to 0.93
	BB′	0.65	1.10 to 1.79

*Average discrepancies in percent.

captured by the Griffin-Pronghorn code system. The external momentum source, buoyancy effects, DNP drift, and temperature feedback are all considered properly in a fully coupled manner. This completes the verification of the steady-state, flowing-fuel simulation capability of the Griffin-Pronghorn code system.

III.C. Phase 2: Multiphysics Transient Benchmark

III.C.1. Step 2.1: Forced Convection Transient

In order to obtain asymptotic power waves, 10 cycles were simulated for each frequency, and the last three cycles were taken to compute the power gain and phase shift. The time step size was set to 50 ms for the lowest frequency case (0.0125 Hz) and reduced inversely proportionally to the frequency with a minimum of 5 ms. Due to the excessive computing time of lower frequency cases, the mesh discretization was reduced to 100 × 100 for the transient analysis.

The average discrepancies of fission rate density along AA′ and BB′ incurred by the coarsening of mesh turned out to be only 0.04% and 0.05%, respectively, in the base steady-state case. Since the integrated reactor power is the only quantity of interest in this transient analysis, using a coarser mesh is considered reasonable. With this time stepping and mesh discretization, the lowest frequency case required 16 080 time steps and took 15 111 CPU hours or about 3.3 calendar days to solve with 192 CPU cores on the INL Sawtooth cluster.

As the perturbation frequency gets higher, it is expected that the power gain will decrease (i.e., the

TABLE XXIV

Step 1.4—Reactivity Change from Step 0.2

	U_{lid} (m/s)	$\rho - \rho_{0.2}$ (pcm)				
		P (GW)				
		0.2	0.4	0.6	0.8	1.0
Average (standard deviation)	**0.0**	−264.3 (3.4)	−499.3 (6.3)	−732.8 (8.6)	−969.3 (10.9)	−1212.7 (15.2)
Griffin		−263.4	−499.3	−733.3	−970.4	−1212.0
Difference		0.9	0.0	−0.5	−1.1	0.7
Average (standard deviation)	**0.1**	−267.1 (3.7)	−499.9 (6.3)	−732.6 (8.7)	−969.2 (11.4)	−1211.6 (15.0)
Griffin		−265.6	−499.6	−733.0	−969.8	−1211.0
Difference		1.5	0.3	−0.4	−0.6	0.6
Average (standard deviation)	**0.2**	−269.8 (4.4)	−500.0 (6.2)	−731.3 (8.6)	−966.7 (11.2)	−1208.5 (14.9)
Griffin		−267.7	−499.7	−731.8	−966.8	−1208.0
Difference		2.1	0.3	−0.5	−0.1	0.5
Average (standard deviation)	**0.3**	−270.8 (4.8)	−500.1 (6.3)	−730.2 (8.8)	−964.1 (11.3)	−1204.5 (15.1)
Griffin		−269.5	−499.3	−730.0	−963.9	−1203.8
Difference		1.3	0.8	0.2	0.2	0.7
Average (standard deviation)	**0.4**	−273.7 (4.9)	−500.1 (6.5)	−729.2 (9.1)	−961.7 (11.5)	−1200.7 (15.2)
Griffin		−271.3	−499.1	−728.5	−961.3	−1200.0
Difference		2.4	1.0	0.7	0.4	0.7
Average (standard deviation)	**0.5**	−276.0 (5.5)	−500.9 (7.2)	−728.7 (9.6)	−960.5 (12.3)	−1197.8 (15.4)
Griffin		−273.5	−499.1	−727.5	−959.3	−1196.9
Difference		2.5	1.8	1.2	1.2	0.9

TABLE XXV

Step 1.4—Number of Picard Iterations and Run times

	U_{lid} (m/s)	P (GW)				
		0.2	0.4	0.6	0.8	1.0
Number of iterations	**0.0**	3	3	3	3	5
Griffin runtime (s)		30	30	30	30	44
Pronghorn run time (s)		1122	1158	1183	1205	1780
Number of iterations	**0.1**	3	3	3	3	5
Griffin run time (s)		30	30	30	30	44
Pronghorn run time (s)		1111	1183	1217	1190	1811
Number of iterations	**0.2**	3	3	3	5	5
Griffin run time (s)		30	30	30	41	43
Pronghorn run time (s)		1168	1199	1210	1696	1895
Number of iterations	**0.3**	3	3	3	5	5
Griffin run time (s)		31	31	31	41	43
Pronghorn run time (s)		1186	1235	1288	1873	1937
Number of iterations	**0.4**	3	3	3	5	5
Griffin run time (s)		30	31	30	41	44
Pronghorn run time (s)		1168	1213	1263	1855	1909
Number of iterations	**0.5**	3	3	3	5	5
Griffin run time (s)		31	31	31	42	45
Pronghorn run time (s)		1149	1266	1278	1865	1935

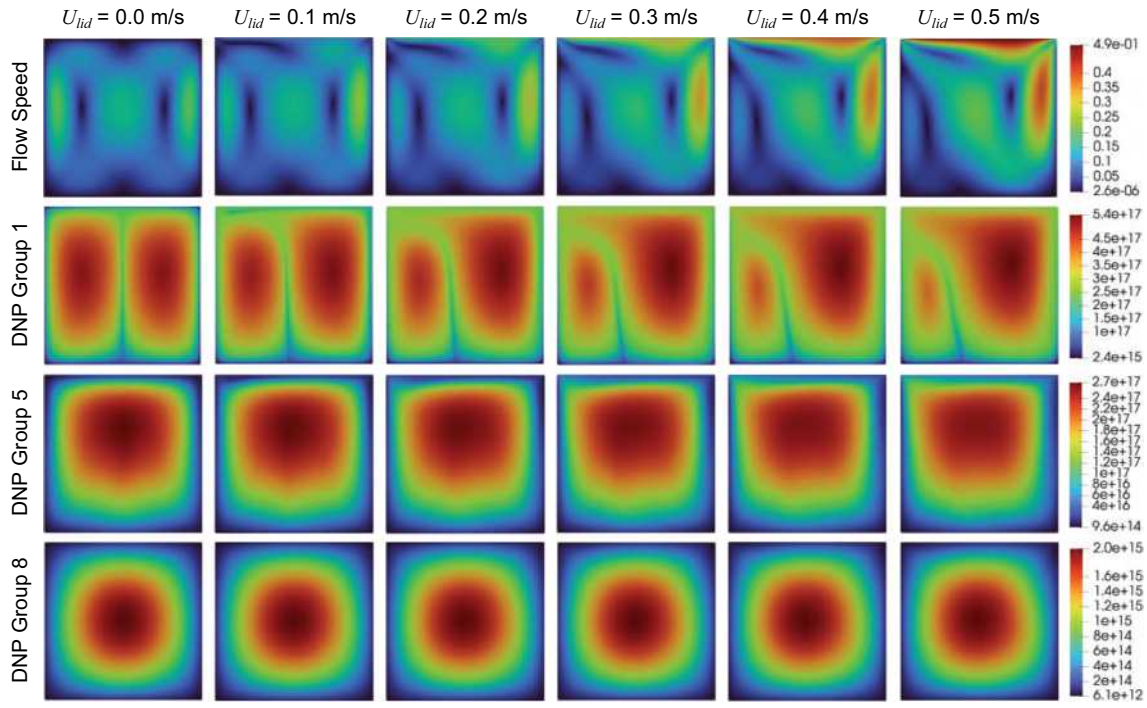

Fig. 15. Step 1.4—Flow speed (m/s) and DNP density (1/m^3) depending on the lid velocity.

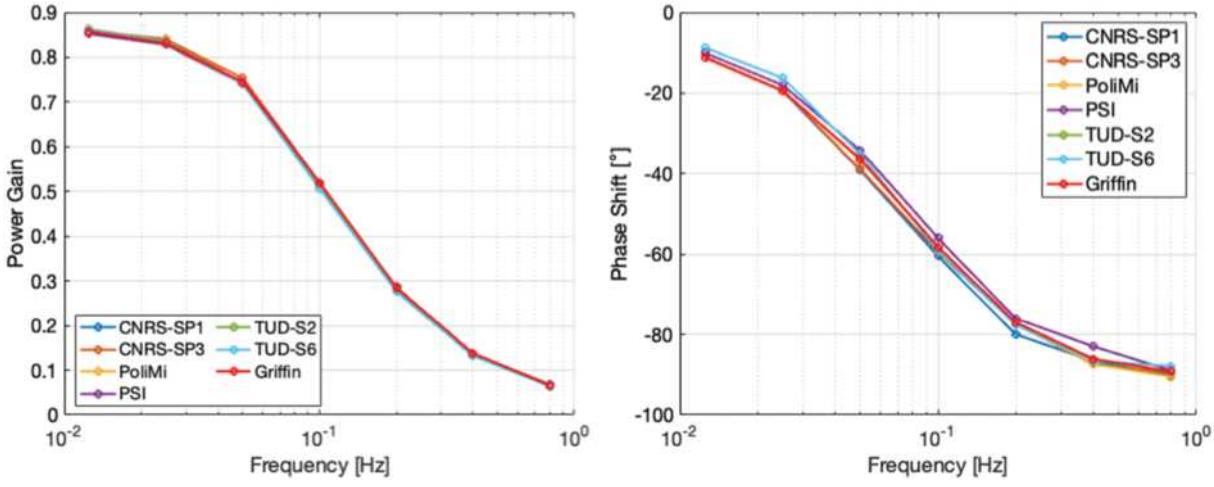

Fig. 16. Step 2.1—(left) Power gain and (right) phase shift as a function of frequency.

amplitude of the power wave is reduced) and the phase shift will approach −90 deg, as displayed by the results. Figure 16 presents the power gain and phase shift of Griffin and the reference codes, and the discrepancies are summarized in Table XXVI. Figure 17 demonstrates the behavior of the power and heat transfer coefficient waves of the 0.0125-Hz and 0.8-Hz cases as an example. For the power gain, the discrepancies are within the standard deviation of the reference values except at 0.1 Hz where the discrepancy of 0.93% is slightly above the standard deviation of 0.86%.

For the phase shift, the discrepancies increase to 7% to 10% in the lowest frequencies. However, the reference values are highly scattered, and the discrepancies still fall within the standard deviations at all points. The estimation of power gain and phase shift should be done after the power wave is fully saturated, but there might be differences between each code on how to determine the saturation. Different time stepping of

TABLE XXVI

Step 2.1—Summary of Power Gain and Phase Shift Discrepancies

Observable		Frequency (Hz)						
		0.0125	0.025	0.05	0.1	0.2	0.4	0.8
Power gain	Average	0.8597	0.8352	0.7464	0.5150	0.2821	0.1360	0.0659
	Griffin	0.8572	0.8307	0.7446	0.5198	0.2851	0.1376	0.0665
	Difference (%)	−0.29	−0.54	−0.24	0.93	1.05	1.16	0.92
	Standard Deviation (%)	0.45	0.52	0.86	0.86	1.19	1.64	2.50
Phase shift (deg)	Average	−10.113	−18.103	−36.480	−58.778	−77.678	−86.297	−89.160
	Griffin	−11.118	−19.408	−36.314	−58.175	−76.971	−86.123	−89.249
	Difference (%)	9.93	7.20	−0.45	−1.03	−0.91	−0.20	0.10
	Standard Deviation (%)	11.43	8.69	5.70	2.60	1.64	1.92	1.27

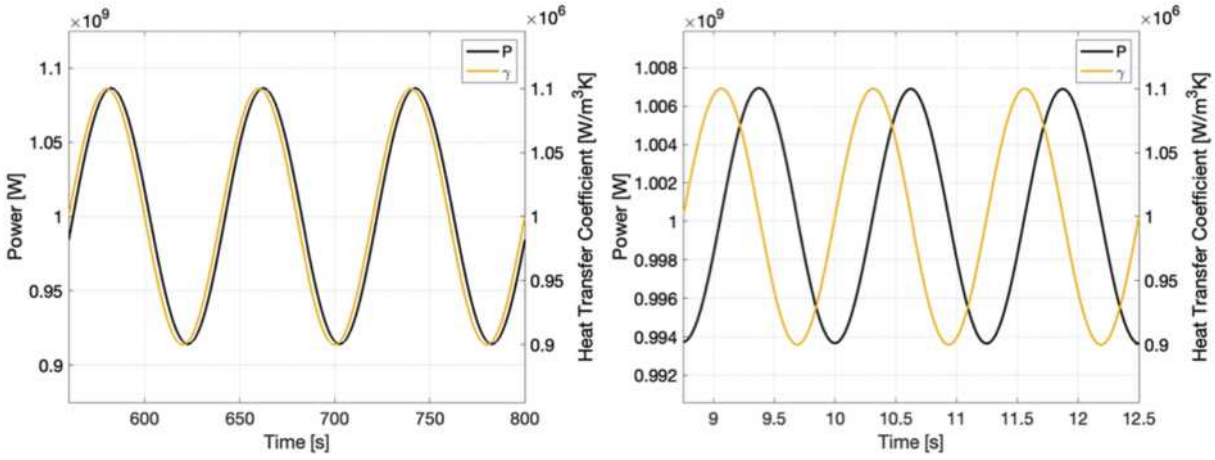

Fig. 17. Step 2.1—Power and heat transfer coefficient waves for (left) 0.0125 Hz and (right) 0.8 Hz.

each code can also contribute to the differences. However, it is clear that the Griffin solutions present consistent trends with the reference codes, and therefore, we conclude that the Griffin-Pronghorn code system is sound for fully coupled transient simulations as well.

IV. CONCLUSION

In this work, the MSR flowing-fuel simulation capability of the Griffin-Pronghorn-coupled multiphysics code system of INL was verified against the CNRS MSR benchmark problem. In the coupled code system, Pronghorn solves the generation, decay, and transport of DNPs as well as the fluid velocity and temperature fields based on the fission rate and heat provided by Griffin, and the fluid temperature and DNP distributions are fed back to Griffin. The coupling is enabled by the underlying MOOSE framework through its MultiApp system.

The benchmark problem encompasses both single and multiphysics and both steady-state and transient conditions, and the Griffin-Pronghorn code system showcased the expected physics phenomena and produced consistent results with the reference codes under all conditions. Relatively large discrepancies were observed in the fission rate density at the boundaries during standalone neutronics solution verification (step 0.2), which affected all the downstream solutions. This is believed to be due to an insufficient mesh discretization of the reference codes. This was indirectly demonstrated by conducting a mesh refinement using a piecewise constant shape function in Griffin. The piecewise constant shape function required more than eight times finer mesh to yield an equivalent solution with a linear shape function, which is the default scheme of Griffin. Apart from this, the Griffin-Pronghorn code system demonstrated good agreement with the reference codes in all the benchmark cases.

This work is part of a larger verification and validation effort for the Griffin-Pronghorn code system toward more complex and realistic MSR problems. The Griffin-Pronghorn code system is currently being validated against the actual experimental data of the MSRE[34] and is being utilized for a preliminary analysis of the Molten Chloride Reactor Experiment (MCRE), which will be built at INL by TerraPower and Southern Company. Future efforts will continue the verification and validation of the Griffin-Pronghorn code system for a wider variety of benchmarks and experiments to demonstrate its application to practical MSR designs.

Acknowledgments

This paper was authored at INL by Battelle Energy Alliance LLC, operator of INL under contract no. DE-AC07-05ID14517 with the U.S. Department of Energy (DOE). The work was sponsored by the National Reactor Innovation Center as part of the Virtual Test Bed project. The research made use of the resources of the High-Performance Computing Center at INL, which is supported by the Office of Nuclear Energy of the DOE and the Nuclear Science User Facilities under contract no. DE-AC07-05ID14517.

Disclosure Statement

No potential conflict of interest was reported by the authors.

Funding

This work was supported by the Office of Nuclear Energy, U.S. Department of Energy [DE-AC07-05ID14517].

Nomenclature

C_k = concentration of DNP of family k

c_p = specific heat

D = salt turbulent diffusion coefficient

D_g = neutron diffusion coefficient of energy group g

g = neutron energy group index, $g = 1, 2, \cdots, G$

$\vec{g}$ = gravitational force vector

k = DNP family index, $k = 1, 2, \cdots, K$

k_{eff} = effective multiplication factor or eigenvalue of the problem

P = total power

p = pressure

q''' = heat source density

S_c = Schmidt number

T = fluid temperature

T_0 = reference fluid temperature

t = time variable

U_{lid} = lid-velocity

$\vec{u}$ = velocity vector

$\bar{\nu}$ = number of neutrons emitted per fission

ν = kinematic viscosity

Greek

α = thermal expansion coefficient

β_k = delayed neutron fraction of family k

γ = volumetric heat transfer coefficient

λ_k = decay constant of precursor family k

κ_f = thermal conductivity

v_g = neutron velocity of energy group g

ρ = reactivity

ρ = fluid density

$\Sigma_{x,g}$ = cross section of type x and energy group g; t = total, f = fission, and s = scattering

ϕ_g = neutron scalar flux of energy group g

$\chi^k_{d,g}$ = fraction of delayed neutrons emitted into the energy group g from precursor family k

$\chi_{p,g}$ = fraction of prompt neutrons emitted into the energy group g

References

1. "A Technology Roadmap for Generation IV Nuclear Energy Systems," GIF-002-00, U.S. Department of Energy, Nuclear Energy Research Advisory Committee, and the Generation IV International Forum (2002).
2. E. S. BETTIS et al., "The Aircraft Reactor Experiment—Design and Construction," *Nucl. Sci. Eng.*, **2**, *6*, 804 (1957); https://doi.org/10.13182/NSE57-A35495.
3. P. N. HAUBENREICH and J. R. ENGEL, "Experience with the Molten-Salt Reactor Experiment," *Nucl. Appl. Technol.*, **8**, *2*, 118 (1970); https://doi.org/10.13182/NT8-2-118.
4. T. W. KERLIN, S. J. BALL, and R. C. STEFFY, "Theoretical Dynamics Analysis of the Molten-Salt Reactor Experiment," *Nucl. Technol.*, **10**, *2*, 118 (1971); https://doi.org/10.13182/NT71-A30920.
5. M. DELPECH et al., "Benchmark of Dynamic Simulation Tools for Molten Salt Reactors," *Proc. GLOBAL 2003*, p. 2182, New Orleans, Louisiana, November 16–20, 2003, American Nuclear Society (2003).
6. M. BROVCHENKO et al., "Optimization of the Pre-conceptual Design of the MSFR," R_EVOL_D2.2, Evaluation and Viability of Liquid Fuel Fast Reactor System Project (2013).
7. E. MERLE-LUCCOTE et al., "Launching the Thorium Fuel Cycle with the Molten Salt Fast Reactor," *Proc. ICAPP 2011*, Nice, France, May 2–5, 2011, p. 842, Societe Francaise d'Energie Nucleaire (2011).
8. K. J. KRAMER et al., "TerraPower's Molten Chloride Fast Reactor Technology," presented at the ETEC Nuclear Suppliers Workshop, Knoxville, Tennessee, October 2, 2018, Oak Ridge National Laboratory (2018).
9. H. YAMANO et al., "SIMMER-III: A Computer Program for LMFR Core Disruptive Accident Analysis—Version 3.A Model Summary and Program Description," JNC-TN9400-2003-071, Japan Nuclear Cycle Development Institute (2003).
10. D. LECARPENTIER and V. CARPENTIER, "A Neutronics Program for Critical and Nonequilibrium Study of Mobile Fuel Reactors: The Cinsf1D Code," *Nucl. Sci. Eng.*, **143**, *1*, 33 (2003); https://doi.org/10.13182/NSE03-A2316.
11. J. KREPEL et al., "DYN3D-MSR Spatial Dynamics Code for Molten Salt Reactors," *Ann. Nucl. Energy*, **34**, *6*, 449 (2007); https://doi.org/10.1016/j.anucene.2006.12.011.
12. K. ZHUANG et al., "Improvements and Validation of the Transient Analysis Code MOREL for Molten Salt Reactors," *Nucl. Sci. Technol.*, **54**, *8*, 878 (2017); https://doi.org/10.1080/00223131.2017.1323689.
13. "COMSOL Multiphysics Simulation Software," COMSOL; https://www.comsol.com/comsol-multiphysics.
14. B. BOER et al., "Validation of the DALTON-THERMIX Code System with Transient Analyses of the HTR-10 and

Application to the PBMR," *Nucl. Technol.*, **170**, *2*, 306 (2010); https://doi.org/10.13182/NT10-A9485.

15. S. J. DE ZWAAN et al., "Static Design of a Liquid-Salt-Cooled Pebble Bed Reactor (LSPBR)," *Ann. Nucl. Energy*, **34**, *1–2*, 83 (2007); https://doi.org/10.1016/j.anucene.2006.11.008.
16. E. E. PETTERSEN, "Coupled Multi-Physics Simulations of the Molten Salt Fast Reactor Using Coarse-Mesh Thermal-Hydraulics and Spatial Neutronics," MS Thesis, Engineering and System Sciences, Paris-Saclay University (Sep. 2016).
17. "OpenFOAM, Open Source Computation Fluid Dynamics," CFD Direct, Ltd; https://cfd.direct/openfoam/.
18. M. AUFIERO et al., "Development of an OpenFOAM Model for the Molten Salt Fast Reactor Transient Analysis," *Chem. Eng. Sci.*, **111**, 390 (2014); https://doi.org/10.1016/j.ces.2014.03.003.
19. Z. MAUSOLFF, M. DEHART, and S. GOLUOGLU, "Design and Assessment of a Molten Chloride Fast Reactor," *Nucl. Eng. Des.*, **379**, 111181 (2021); https://doi.org/10.1016/j.nucengdes.2021.111181.
20. T. FEI et al., "MSRE Transient Benchmarks Using SAM," *EPJ Web Conf.*, **247**, 07008 (2021); https://doi.org/10.1051/epjconf/202124707008.
21. A. LINDSAY et al., "Introduction to Moltres: An Application for Simulation of Molten Salt Reactors," *Ann. Nucl. Energy*, **114**, 530 (2018); https://doi.org/10.1016/j.anucene.2017.12.025.
22. Y. S. JUNG et al., "Molten Salt Reactor Analysis Capability of PROTEUS-NODAL," *Trans. Am. Nucl. Soc.*, **119**, 1131, Orlando, Florida, November 11–15, 2018, American Nuclear Society (2018).
23. M. K. JARADAT et al., "Molten Salt Reactor Transient Analysis Capability of PROTEUS-NODAL," *Proc. GLOBAL 2019*, Seattle, Washington, September 22–27, 2019, p. 930, American Nuclear Society (2019).
24. M. K. JARADAT and W. S. YANG, "An Adaptive Time-Stepping Control Algorithm for Molten Salt Reactor Transient Analyses," *Ann. Nucl. Energy*, **190**, 109880 (2023); https://doi.org/10.1016/j.anucene.2023.109880.
25. M. K. JARADAT et al., "Development and Validation of PROTEUS-NODAL Transient Analyses Capabilities for Molten Salt Reactors," *Ann. Nucl. Energy*, **160**, 108402 (2021); https://doi.org/10.1016/j.anucene.2021.108402.
26. G. YANG et al., "Development of Coupled PROTEUS-NODAL and SAM Code System for Multiphysics Analysis of Molten Salt Reactors," *Ann. Nucl. Energy*, **168**, 108889 (2022); https://doi.org/10.1016/j.anucene.2021.108889.
27. C. LEE et al., "Griffin Software Development Plan," INL/EXT-21-63185 and ANL/NSE-21/23, Idaho National Laboratory and Argonne National Laboratory (2021).
28. A. J. NOVAK et al., "Pronghorn: A Multidimensional Coarse-Mesh Application for Advanced Reactor Thermal Hydraulics," *Nucl. Technol.*, **207**, *7*, 1015 (2021); https://doi.org/10.1080/00295450.2020.1825307.
29. A. D. LINDSAY et al., "2.0—MOOSE: Enabling Massively Parallel Multiphysics Simulation," *SoftwareX*, **20**, 101202 (2022); https://doi.org/10.1016/j.softx.2022.101202.
30. P. BALESTRA et al., "Coupled Multiphysics Simulation of Pool-Type Molten Salt Reactors Using Griffin/Pronghorn," *Trans. Am. Nucl. Soc.*, **123**, 1587, Virtual, November 16–19, 2020, American Nuclear Society (2020).
31. P. BALESTRA et al., "Multiphysics Simulation of the Molten-Salt Fast Reactor Using Griffin and Pronghorn," *Proc. M&C 2021*, Virtual, October 3–7, 2021, p. 2382, American Nuclear Society (2021).
32. A. ABOU-JAOUDE et al., "A Workflow Leveraging MOOSE Transient Multiphysics Simulations to Evaluate the Impact of Thermophysical Property Uncertainties on Molten-Salt Reactors," *Ann. Nucl. Energy*, **163**, 108546 (2021); https://doi.org/10.1016/j.anucene.2021.108546.
33. M. TIBERGA et al., "Results from a Multi-Physics Numerical Benchmark for Codes Dedicated to Molten-Salt Fast Reactors," *Ann. Nucl. Energy*, **142**, 107428 (2020); https://doi.org/10.1016/j.anucene.2020.107428.
34. M. K. JARADAT and J. ORTENSI, "Thermal Spectrum Molten Salt-Fueled Reactor Reference Plant Model," INL/RPT-23-72875, Idaho National Laboratory (2023).
35. D. R. GASTON et al., "Physics-Based Multiscale Coupling for Full Core Nuclear Reactor Simulation," *Ann. Nucl. Energy*, **84**, *45*, 45 (2015); https://doi.org/10.1016/j.anucene.2014.09.060.
36. Y. WANG et al., "Rattlesnake: A MOOSE-Based Multiphysics Multischeme Radiation Transport Application," *Nucl. Technol.*, **207**, *7*, 1047 (2021); https://doi.org/10.1080/00295450.2020.1843348.
37. F. GLEICHER et al., "The Coupling of the Neutron Transport Application RATTLESNAKE to the Fuels Performance Application BISON under the MOOSE Framework," *Proc. PHYSOR 2014*, 1106401, Kyoto, Japan, September 28–October 3, 2014, Japan Atomic Energy Agency (2014).
38. Y. S. JUNG, C. LEE, and M. A. SMITH, "PROTEUS-MOC User Manual," ANL/NE-18/10, Argonne National Laboratory (2018).
39. C. LEE and W. S. YANG, "MC^2-3: Multigroup Cross Section Generation Code for Fast Reactor Analysis," *Nucl. Sci. Eng.*, **187**, *3*, 268 (2017); https://doi.org/10.1080/00295639.2017.1320893.
40. J. W. PETERSON, A. D. LINDSAY, and F. KONG, "Overview of the Incompressible Navier-Stokes Simulation Capabilities in the MOOSE Framework," *Adv. Eng. Software*, **119**, 68 (2018); https://doi.org/10.1016/j.advengsoft.2018.02.004.

41. F. MOUKALLED, L. MANGANI, and M. DARWISH, *The Finite Volume Method in Computational Fluid Dynamics*, Springer International (2015).

42. M. AUFIERO, "Serpent-OpenFOAM Coupling for Criticality Accidents Modelling—Definition of a Benchmark for MSRs Multiphysics Modelling," presented at the Serpent and Multiphysics Workshop, Grenoble, France, February 26–27, 2015, Laboratoire de Physique Subatomique et de Cosmologie (2015).

43. M. AUFIERO and P. RUBIOLO, "Testing and Verification of Multiphysics Tools for Fast-Spectrum MSRs: The CNRS Benchmark," *Trans. Am. Nucl. Soc*., **118**, 837, Philadelphia, Pennsylvania, June 17–21, 2018, American Nuclear Society (2018).

44. J. A. BLANCO, P. RUBIOLO, and E. DUMONTELI, "Neutronic Modeling Strategies for a Liquid Fuel Transient Calculation," *EPJ Web Conf.*, **247**, 06013 (2021); https://doi.org/10.1051/epjconf/202124706013.

45. E. CERVI et al., "Development of an SP_3 Neutron Transport Solver for the Analysis of the Molten Salt Fast Reactor," *Nucl. Eng. Des.*, **346**, 209 (2019); https://doi.org/10.1016/j.nucengdes.2019.03.001.

46. C. FIORINA et al., "GeN-Foam: A Novel OpenFOAM® Based Multi-Physics Solver for 2D/3D Transient Analysis of Nuclear Reactors," *Nucl. Eng. Des.*, **294**, 24 (2015); https://doi.org/10.1016/j.nucengdes.2015.05.035.

47. M. TIBERGA, D. LATHOUWERS, and J. L. KLOOSTERMAN, "A Discontinuous Galerkin FEM Multi-Physics Solver for the Molten Salt Fast Reactor," *Proc. M&C 2019*, Portland, Oregon, Aug. 25–29, 2019, p. 181, American Nuclear Society (2019).

48. S. V. PATANKAR and D. B. SPALDING, "A Calculation Procedure for Heat, Mass, and Momentum Transfer in Three-Dimensional Parabolic Flows," *Int. J. Heat Mass Transfer*, **15**, *10*, 1787 (1972); https://doi.org/10.1016/0017-9310(72)90054-3.